



JGR Solid Earth

RESEARCH ARTICLE

10.1029/2022JB025174

Key Points:

- Helmholtz tomography applied at ocean-bottom seismometer arrays recovers Rayleigh wave attenuation and site amplification at 20–150 s period
- Synthetic tests show that focusing/defocusing are successfully accounted for, including near the coastline where strong multipathing occurs
- Strong site amplification observed at the Juan de Fuca ridge may be used to improve models of crust and shallow mantle

Supporting Information:

Supporting Information may be found in the online version of this article.

Correspondence to:

J. B. Russell,
joshua_russell@brown.edu

Citation:

Russell, J. B., & Dalton, C. A. (2022). Rayleigh wave attenuation and amplification measured at ocean-bottom seismometer arrays using Helmholtz tomography. *Journal of Geophysical Research: Solid Earth*, 127, e2022JB025174. <https://doi.org/10.1029/2022JB025174>

Received 12 JUL 2022

Accepted 3 OCT 2022

Author Contributions:

Conceptualization: Joshua B. Russell, Colleen A. Dalton

Formal analysis: Joshua B. Russell

Funding acquisition: Joshua B. Russell

Investigation: Joshua B. Russell, Colleen A. Dalton

Methodology: Joshua B. Russell, Colleen A. Dalton

Resources: Colleen A. Dalton

Supervision: Colleen A. Dalton

Writing – original draft: Joshua B. Russell

Russell

© 2022. The Authors.

This is an open access article under the terms of the Creative Commons Attribution License, which permits use, distribution and reproduction in any medium, provided the original work is properly cited.

Rayleigh Wave Attenuation and Amplification Measured at Ocean-Bottom Seismometer Arrays Using Helmholtz Tomography

Joshua B. Russell¹  and Colleen A. Dalton¹ 

¹Department of Earth, Environmental, and Planetary Sciences, Brown University, Providence, RI, USA

Abstract Shear attenuation provides insights into the physical and chemical state of the upper mantle. Yet, observations of attenuation are infrequent in the oceans, despite recent proliferation of arrays of ocean-bottom seismometers (OBSs). Studies of attenuation in marine environments must overcome unique challenges associated with strong oceanographic noise at the seafloor and data loss during OBS recovery in addition to untangling the competing influences of elastic focusing, local site amplification, and anelastic attenuation on surface-wave amplitudes. We apply Helmholtz tomography to OBS data to simultaneously resolve array-averaged Rayleigh wave attenuation and maps of site amplification at periods of 20–150 s. The approach explicitly accounts for elastic focusing and defocusing due to lateral velocity heterogeneity using wavefield curvature. We validate the approach using realistic wavefield simulations at the NoMelt Experiment and Juan de Fuca (JdF) plate, which represent endmember open-ocean and coastline-adjacent environments, respectively. Focusing corrections are successfully recovered at both OBS arrays, including at periods <35 s at JdF where coastline effects result in strong multipathing. When applied to real data, our observations of Rayleigh wave attenuation at NoMelt and JdF revise previous estimates. At NoMelt, we observe a low attenuation lithospheric layer ($Q_\mu > 1,500$) overlying a highly attenuating asthenospheric layer ($Q_\mu \sim 50$ to 70). At JdF, we find a broad peak in attenuation ($Q_\mu \sim 50$ to 60) centered at a depth of 100–130 km. We also report strong local site amplification at the JdF Ridge (>10% at 31 s period), which can be used to refine models of crust and shallow mantle structure.

Plain Language Summary Seismic tomography provides a tool for probing regions deep within the Earth that are otherwise inaccessible. The degree to which seismic waves lose energy as they travel (seismic attenuation) provides information about temperature and melt in Earth's interior. However, seismic attenuation is notoriously difficult to measure due to complicating effects on wave amplitudes from focusing and amplification of the waves as they travel through the heterogeneous Earth. Here we introduce a tool that utilizes both amplitude and travel-time information observed across arrays of seismometers to account for these competing effects and accurately quantify seismic attenuation. We validate the approach using realistic simulations and apply it to real data sets at young (~3 Myr) and older (~70 Myr) locations in the Pacific Ocean. Our observations revise previous estimates of attenuation at the two locations, revealing high attenuation that extends deeper beneath the Juan de Fuca ridge than previously thought and high attenuation in the asthenosphere beneath the typical oceanic plate. These observations have important implications for our understanding of mantle temperature and melt content beneath the oceans.

1. Introduction

Shear attenuation of the upper mantle is a key parameter for quantifying the physical and chemical state of the asthenosphere. As attenuation and shear velocity respond differently to variations in temperature, melt fraction, grain size, and volatile content (Faul & Jackson, 2005; Jackson & Faul, 2010; McCarthy & Takei, 2011; McCarthy et al., 2011; Yamauchi & Takei, 2016), jointly interpreting these two observables offers unprecedented constraints on upper mantle properties (Dalton & Faul, 2010; Debayle et al., 2020; Havlin et al., 2021; Priestley & McKenzie, 2013; Richards et al., 2020). In contrast to shear velocity, which is routinely constrained at local and regional scales, our understanding of upper-mantle attenuation is largely limited to global models derived from Rayleigh wave observations (e.g., Adenis et al., 2017a, 2017b; Dalton et al., 2008; Karaoglu & Romanowicz, 2018). This is especially true of the ocean basins where station coverage is sparse compared

Writing – review & editing: Joshua B. Russell, Colleen A. Dalton

to the continents. In global models, shear attenuation beneath the ocean basins is primarily constrained by basin-traversing Rayleigh waves with long ray paths that tend to smear structure both laterally and vertically.

A primary challenge for all studies of Rayleigh wave attenuation is isolating the signal of attenuation in amplitude measurements from other effects, including source excitation, focusing/defocusing, and local site amplification. While progress has been made at longer periods at the global scale (e.g., Dalton & Ekström, 2006), the ability to robustly account for these effects at higher frequencies at regional and local scales is still a topic of active development (e.g., F. C. Lin et al., 2012; Forsyth & Li, 2005; Yang & Forsyth, 2006). Improving resolution of upper-mantle shear attenuation requires innovative seismic techniques that resolve regional-scale Rayleigh wave attenuation while accurately accounting for these additional factors that complicate wave amplitudes.

New surface-wave imaging techniques have been developed in recent years owing to an abundance of high-quality broadband seismic data sets with dense and uniform station coverage, such as the USArray. These techniques make use of the spatial gradients of Rayleigh wave amplitude and phase to extract structural information from the wavefield. Perhaps the most widely used to date is Helmholtz tomography, which yields regional-scale maps of phase velocity while accounting for finite-frequency effects (F.-C. Lin & Ritzwoller, 2011; Jin & Gaherty, 2015). The approach is attractive due to its simplicity compared to alternatives such as wave gradometry (Langston, 2007a, 2007b, 2007c; Y. Liu & Holt, 2015) and requires fewer physical assumptions about the wavefield compared to simpler techniques such as the two-plane wave (TPW) method, which approximates the wavefield as the superposition of two plane waves with varying phase and amplitude (Forsyth & Li, 2005). Furthermore, the openly available Automated Surface-Wave Measurement System (ASWMS) software package has made Helmholtz tomography widely accessible to the seismology community (Jin & Gaherty, 2015). F. C. Lin et al. (2012) recently developed an extension of Helmholtz tomography for estimating Rayleigh wave attenuation and site amplification, which has been applied to USArray data (Bao et al., 2016; Bowden et al., 2017; F. C. Lin et al., 2012). However, it is not yet clear how effectively the technique can be applied at smaller scale arrays with often less optimal array geometries.

Despite recent methodological advances on land, seismic imaging in marine environments lags due to challenges associated with the relatively noisy seafloor environment and often sparse station coverage compared to terrestrial seismic deployments. This is true especially for studies of Rayleigh wave attenuation across arrays of ocean-bottom seismometers (OBSs), where only a handful of observations have been made to date (e.g., Ma et al., 2020; Ruan et al., 2018; Saikia et al., 2021; Yang & Forsyth, 2006). To our knowledge, all existing regional Rayleigh wave attenuation observations made in the oceans were measured using the TPW method. While TPW provides a simple approach for measuring 1-D Rayleigh wave attenuation in the presence of weak or moderate multipathing, it may suffer in complex regions such as near the coastlines, where the wavefield may not be well approximated by two interfering plane waves. Furthermore, we are unaware of any previous reports of Rayleigh wave site amplification in the oceans, despite having sensitivity to elastic structure that complements that of phase velocity (F. C. Lin et al., 2012; Schardong et al., 2019). Helmholtz tomography offers a promising approach that can simultaneously constrain attenuation and site amplification while accurately accounting for wavefield focusing/defocusing. However, it is unclear whether typical OBS array geometries and earthquake distributions offer the resolution needed for the technique to be successful as all previous applications have used well-behaved USArray data.

In this study, we show that Helmholtz tomography can be used to reliably measure array-averaged Rayleigh wave attenuation and 2-D maps of site amplification in oceanic settings, offering an alternative to the TPW method. We validate the approach using realistic wavefield simulations through 3-D elastic structure, demonstrating its ability to account for focusing/defocusing and recover attenuation and amplification. The methodology is applied at two OBS arrays representing endmember locales (open ocean and coastline adjacent) with apertures on the order of 500 km × 500 km. Our observations revise previous estimates of Rayleigh wave attenuation at the two locations and provide perhaps the first measurements of site amplification in an oceanic setting. We implement the approach as an add-on to the ASWMS software, offering a new tool for estimating Rayleigh wave attenuation and amplification across regional-scale arrays that has been validated by realistic synthetic seismograms.

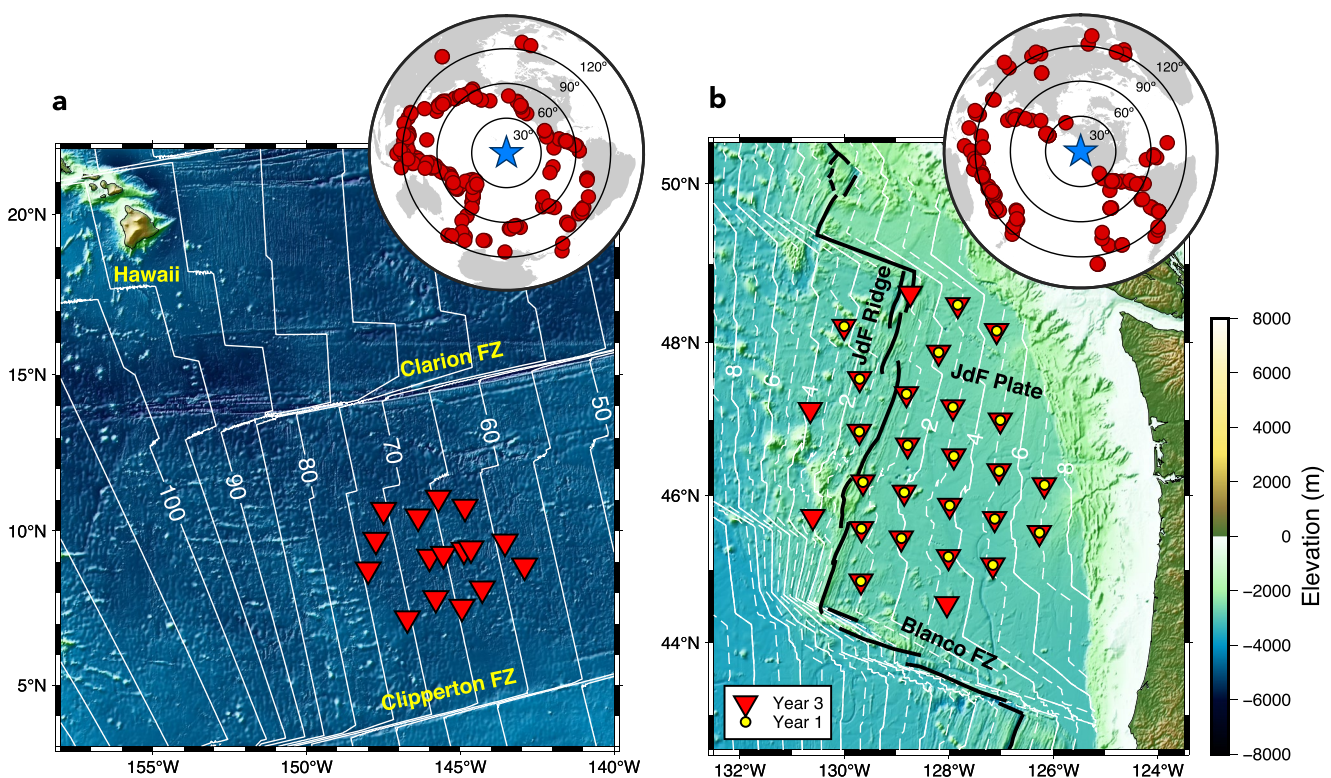


Figure 1. Maps of station locations for the (a) NoMelt experiment and (b) Juan de Fuca (JdF) component of the Cascadia Initiative. Event locations are shown at the top right of each panel. Seafloor age contours (white; labels in Myr) are from Seton et al. (2020). FZ = fracture zone. This figure was made using PyGMT (Uieda et al., 2022).

2. Data and Measurements

Broadband waveform data are utilized from the NoMelt Experiment and the Juan de Fuca (JdF) portion of the Cascadia Initiative, located in the central and eastern Pacific, respectively (Figure 1). The NoMelt experiment was positioned approximately 1,600 km southeast of Hawaii on unperturbed, ~70 Ma seafloor far from hotspot, ridge, or subduction influences (Ma et al., 2020; Mark et al., 2019; P.-Y. P. Lin et al., 2016; Russell et al., 2019, 2022). The experiment consisted of a reflection/refraction survey (Mark et al., 2019), a magnetotelluric deployment (Sarafian et al., 2015), and a broadband OBS deployment from December 2012 to December 2013 (Ma et al., 2020; Mark et al., 2021; P.-Y. P. Lin et al., 2016; Russell et al., 2019, 2022). Here, we make use of the 16 broadband OBS with an array aperture of 400 km × 600 km. Station depths range from 4,889 to 5,331 m below the sea surface.

The Cascadia Initiative was an amphibious experiment consisting of a multi-year broadband OBS deployment spanning the JdF and Gorda plates (Bell et al., 2016; Byrnes et al., 2017; Eilon & Forsyth, 2020; Hawley et al., 2016; Janiszewski et al., 2019; Ruan et al., 2018). We use data from the year 1 (23 stations; November 2011–May 2012) and year 3 (27 stations; August 2013–May 2014) deployments co-located on the JdF plate seaward of the trench. Here, water depth ranges from 2,544 to 2,940 m. We avoid stations in shallow water near the continental shelf due to noisier conditions and crust and mantle structure that is complicated by subduction processes (Janiszewski et al., 2019). While the majority of the 400 km × 400 km deployment footprint is characterized by nascent oceanic plate (~3 Ma average seafloor age), the JdF Ridge cuts NNE-SSW across the western edge of the array (Figure 1b).

The NoMelt and JdF regions represent endmembers in terms of their seafloor age, structural complexity, and noise environment. The NoMelt experiment exemplifies an ideal OBS deployment for Rayleigh wave imaging. Its location in the center of the plate provides excellent azimuthal coverage for teleseismic Rayleigh waves, and the deep (~5,000 m depth) open-ocean environment offers relatively quiet noise conditions. As most paths from source to receiver consist of largely homogeneous oceanic material, most arriving Rayleigh waves show little to

no evidence of multipathing (Ma et al., 2020). In contrast, JdF represents a more challenging coastal environment. The region is characterized by shallower water depths ($\sim 2,700$ m) with higher noise levels and has azimuthal gaps in teleseismic earthquakes to the south and northeast. Additionally, large lateral gradients in velocity structure associated with the continent-ocean transition can produce complex Rayleigh waveforms exhibiting multipathing and scattering, particularly for waves traveling parallel to the coastline (Bell et al., 2016). These differences between the two focus sites allow us to test the limitations of the imaging approach.

We retrieve four-component (3 directional and differential pressure-gauge) data for earthquakes in the Global Centroid Moment Tensor catalog (Ekström et al., 2012) with $M_w > 5.5$, depths < 50 km, and epicentral distances ranging from 20° to 100° . Events with epicentral distances $> 100^\circ$ are avoided as they are more likely to have complicated paths (i.e., large portions that pass through continents), and Rayleigh wave phase and amplitude measurements for distances $> 120^\circ$ can be contaminated by major arc overtones (Hariharan et al., 2020). Although fundamental-mode Rayleigh wave excitation typically peaks at depths < 50 km, our data set could be expanded in the future by considering deeper (primarily vertical dip-slip) earthquakes with considerable excitation below 50 km (Hariharan et al., 2022). As a rough initial quality control metric, we consider only events for which the vertical component Rayleigh wave appears at more than five stations with a signal-to-noise ratio (SNR) > 3 in the period band 20–80 s. In total, these criteria yielded 191 earthquakes for the NoMelt data set and 160 earthquakes for JdF. That more events meet these criteria at NoMelt, which was deployed nearly half as long as JdF, is largely a result of the lower noise levels at those stations.

2.1. Noise Corrections

Vertical component OBS data is often contaminated by tilt and compliance noise. Bottom-current noise typically contaminates the horizontal channels but can appear on the vertical channel as tilt noise if the instrument is slightly rotated from vertical (Crawford & Webb, 2000). Compliance noise results from long-period infragravity waves that produce pressure perturbations at the seafloor (Webb & Crawford, 1999). Both tilt and compliance noise typically dominate at periods > 80 s (depending on water depth) and therefore must be removed in order to make robust long-period surface-wave measurements. Tilt and compliance noise are removed from each vertical channel seismogram by applying the Automated Tilt and Compliance Removal software package (Janiszewski et al., 2019). This tool employs the methodology developed by Crawford and Webb (2000) to estimate and remove coherent signals between the vertical and two horizontal channels and the vertical and pressure channel.

2.2. Phase and Amplitude Measurements

Rayleigh wave phase and amplitude are measured using the ASWMS software package, described in detail by Jin and Gaherty (2015). The tool employs a cross-correlation based approach to measure frequency-dependent interstation phase and group delay times and single-station amplitudes, and here we summarize the procedure. Each waveform is prefiltered using a second-order Butterworth filter with corner frequencies at $\pm 25\%$ of the maximum and minimum frequencies of interest. After prefiltering and windowing each seismogram around the Rayleigh wave arrival using an automated procedure, cross-correlations are calculated between all station pairs within each array. Cross-correlations with a correlation coefficient < 0.65 are discarded. The remaining cross-correlation functions are narrow band filtered, and a five parameter Gaussian wavelet is fit at each frequency, yielding frequency-dependent interstation phase and group travel times, $\delta\tau_{ij}$ and $\delta\tau_{ij}^g$, for each station pair (i, j). Frequency-dependent amplitude measurements, A_i , are obtained at a single station by applying the same Gaussian wavelet fitting procedure to the autocorrelation function and taking the square root of the wavelet amplitude. This procedure is implemented in two overlapping frequency bands from 20 to 84 s and 73 to 150 s, resulting in measurements made at 15 periods between 20 and 150 s.

3. Methods

This section outlines the main equations governing our approach for estimating Rayleigh wave attenuation and site amplification using observations of phase and amplitude. The methodology is implemented as an add-on to the ASWMS software (see Data Availability Statement).

3.1. Helmholtz Tomography

In its most common application, Helmholtz tomography (sometimes referred to as wavefront tracking) offers a method to solve for Rayleigh wave phase velocity maps, $c(x, y)$, where x is longitude and y is latitude, from observations of phase delay, $\tau(x, y)$, and amplitude, $A(x, y)$ (F.-C. Lin & Ritzwoller, 2011; Jin & Gaherty, 2015). More recently, this technique has been extended for measuring Rayleigh wave attenuation and amplification at the USArray (Bao et al., 2016; F. C. Lin et al., 2012). Here, we briefly outline the main equations that govern the approach, relying heavily on the original derivation by F. C. Lin et al. (2012).

Consider a 2-D surface wave potential of the form $\chi(x, y, t) = A(x, y)\beta(x, y)^{-1}\exp\{i\omega(t - \tau(x, y))\}$. This surface-wave potential satisfies the 2-D homogeneous damped wave equation (Tromp & Dahlen, 1992) and balancing the real and imaginary parts yields the following two equations, respectively:

$$\frac{1}{c(x, y)^2} = \frac{1}{c'(x, y)^2} - \frac{\nabla^2(A(x, y)/\beta(x, y))}{\omega^2(A(x, y)/\beta(x, y))} \quad (1)$$

$$\underbrace{2\nabla\tau(x, y) \cdot \frac{\nabla\beta(x, y)}{\beta(x, y)}}_{\text{local amplification gradient}} - \underbrace{\frac{2\alpha(x, y)}{c(x, y)}}_{\text{anelastic attenuation term}} = \underbrace{2\nabla\tau(x, y) \cdot \frac{\nabla A(x, y)}{A(x, y)}}_{\text{apparent amplitude decay}} + \underbrace{\nabla^2\tau(x, y)}_{\text{focusing correction}} \quad (2)$$

where ω is angular frequency, $c'(x, y) = |\nabla\tau(x, y)|^{-1}$ is apparent phase velocity, $c(x, y)$ is structural phase velocity, $\alpha(x, y)$ is the anelastic attenuation coefficient, and $\beta(x, y)$ is relative local site amplification of the surface-wave potential. For brevity, we drop the dependence on position (x, y) for the remainder of this manuscript. The anelastic attenuation parameter α is related to Rayleigh wave attenuation, Q^{-1} , by $\alpha = \omega/2CQ$, where C is group velocity. Because attenuation varies more strongly than group velocity, spatial variations in α should mostly reflect variations in Q^{-1} . Local amplification, β , is a relative measure of local amplitude and is sensitive to depth-dependent elastic structure at the receiver. Values of $\beta > 1$ indicate wave amplification and values of $\beta < 1$ correspond to wave deamplification. As pointed out by Bowden et al. (2017), β represents amplification of the surface-wave potential, which is not directly observable, and therefore it is not strictly equivalent to site amplification determined from more direct methods derived from amplitude ratios (e.g., Eddy & Ekström, 2014, 2020). The two quantities can be related via phase velocity through the expression $A_R/A_{R,0} = \beta\sqrt{c/c_0}$, where A_R is the Rayleigh wave amplification observed at a receiver of interest compared to a reference location $A_{R,0}$, and c/c_0 is the fractional difference in phase velocity relative to the value at the reference location.

Equation 1 with $\beta = 1$ is commonly referred to as the Helmholtz equation and can be used to solve for the structural phase velocity, c , given observations of τ and A (F.-C. Lin & Ritzwoller, 2011). The second term on the right-hand side that includes the Laplacian of the amplitude field normalized by ω^2 accounts for finite-frequency effects. In the high-frequency limit (i.e., ray theory), this term becomes negligible, and Equation 1 reduces to the Eikonal equation (F.-C. Lin et al., 2009). For the purposes of this study, we assume $\beta = 1$ when solving Equation 1 but not when solving Equation 2.

Equation 2 is sometimes referred to as the transport equation and connects unknown quantities β and α on the left-hand side to spatial derivatives of measurable quantities τ and A on the right-hand side. Following the nomenclature of F. C. Lin et al. (2012), the first term on the right-hand side of Equation 2 is the “apparent amplitude decay” in the direction of wave propagation and the second term consisting of the Laplacian of travel time is the “focusing correction.” The entire right-hand side is referred to as the “corrected amplitude decay.” On the left-hand side, we refer to the first and second terms as the “local amplification gradient” and “anelastic attenuation term,” respectively.

Measured surface-wave amplitudes $A(\omega)$ include contributions from earthquake source excitation A_S , local receiver effects A_R , elastic focusing A_F , and amplitude decay due to anelastic attenuation along the ray path A_Q (Dalton & Ekström, 2006):

$$A(\omega) = A_S(\omega) A_R(\omega) A_F(\omega) A_Q(\omega) \quad (3)$$

Isolating the contribution from anelastic attenuation is the primary goal of all attenuation tomography, and in Section 3.2 we describe how our methodology is able to do so. The receiver term, A_R , includes contributions from instrument response, tilt and compliance noise, and local site amplification. The former two contributions are removed prior to making measurements by deconvolving instrument response to displacement and subtracting tilt and compliance noise as described in Section 2.1, respectively. On the other hand, local site amplification, β , that results from energy amplification or deamplification due to elastic structure beneath the receiver, is solved for simultaneously alongside anelastic attenuation. Any imperfections in the instrument response and/or tilt and compliance removal steps at individual stations will map into site amplification and should not greatly affect attenuation measurements.

Elastic focusing and defocusing, A_F , describes horizontal refraction of the wavefield that occurs due to lateral gradients in wavespeed in the Earth. Focusing and defocusing is especially prevalent near the coastlines, where large velocity gradients often exist (e.g., Russell & Gaherty, 2021). This behavior is reflected in the wavefield curvature and is accounted for by the focusing correction term, $\nabla^2\tau$, in Equation 2. However, the $\nabla^2\tau$ term also includes simple geometrical spreading of the 2-D surface-wave wavefield, which results in defocusing and focusing at epicentral distances $<90^\circ$ and $>90^\circ$, respectively, and can be expressed analytically as $\nabla^2\tau_{GS} = (cR \tan X)^{-1}$, where X is epicentral distance in degrees and R is Earth's radius, and the subscript "GS" stands for geometrical spreading (see Text S1 and Figure S2 in Supporting Information S1). Therefore, focusing due only to structural heterogeneity along the ray path is given by

$$\nabla^2\tilde{\tau} = \nabla^2\tau - \nabla^2\tau_{GS} \quad (4)$$

We refer to this quantity as the structural focusing correction term. As it is independent of epicentral distance, this term is informative when considering the overall focusing behavior based on data from many earthquakes (see Section 5.1).

The source term, A_S , includes azimuthal variations in Rayleigh wave amplitude associated with the radiation pattern. Surface waves emitted near nodes in the radiation pattern should be avoided as excitation is both weak and varies rapidly with azimuth. However, this bias has only a small effect on our amplitude data set for three main reasons. First, the governing Equation 2 depends on the amplitude variation in the direction of propagation (i.e., the dot product on the right-hand side), whereas the radiation pattern introduces amplitude variations perpendicular to the propagation direction. Second, the requirement that $\text{SNR} > 3$ as mentioned in Section 2 implicitly removes nodal events from our data set. Third, the relatively small $\sim 500 \text{ km} \times 500 \text{ km}$ array footprint corresponds to only a small azimuthal range for a given teleseismic earthquake. Indeed, even at the larger USArray, Bao et al. (2016) found this bias to be small compared to other sources of error. We tested restricting our data set to source excitation ratios $> 60\%$ of the maximum to explicitly avoid nodes, but we observed no significant improvement (see Figure S3 in Supporting Information S1), and a large portion of the data set was lost ($\sim 50\%$ to 60% of events), degrading azimuthal coverage. For these reasons, we do not explicitly account for source excitation.

3.2. Solving for Attenuation and Site Amplification

The local amplification gradient (first term in Equation 2) depends on propagation azimuth via the dot product with $\nabla\tau$, while the attenuation term containing α is independent of azimuth. To solve for the attenuation coefficient α and amplification β , we follow the curve-fitting approach of Bao et al. (2016). The local amplification gradient term can be expanded as

$$2|\nabla\tau| \left| \frac{\nabla\beta}{\beta} \right| \cos(\theta - \psi_\beta) = 2|\nabla\tau| (\partial_x(\ln\beta)\sin\theta + \partial_y(\ln\beta)\cos\theta) \quad (5)$$

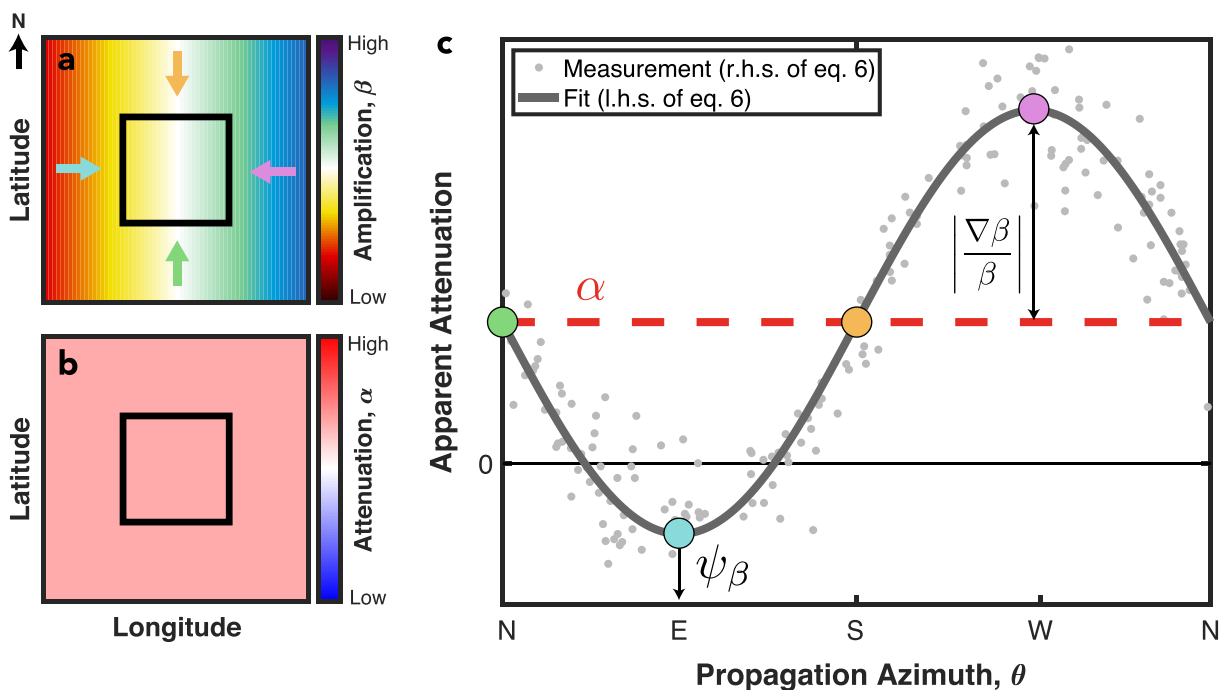


Figure 2. Schematic illustration of Equation 6 for constraining amplification gradient and attenuation. (a) Map of amplification smoothly increasing to the east. Colored arrows show direction of wave propagation for four scenarios indicated by circles in panel (c). The black box represents the region of analysis. (b) Idealized 1-D attenuation map. (c) Apparent attenuation as a function of azimuth that would be measured within the black boxed region using data from many different earthquakes. Each gray dot represents one measurement (with noise, for illustration) for a single earthquake and pixel in the black boxed region. The dark gray curve shows the sinusoidal fit from the left-hand side of Equation 6, and the red dashed line indicates the corresponding attenuation estimate. The large colored circles correspond to each of the cardinal directions of propagation in panel (a).

where θ is the azimuth of wave propagation determined by $\theta = \tan^{-1}(\partial_x \tau / \partial_y \tau)$, and shorthand is used for spatial derivatives: $\partial_x = \partial/\partial x$ and $\partial_y = \partial/\partial y$. The magnitude and azimuth of the local amplification gradient are given by $|\frac{\nabla \beta}{\beta}| = \sqrt{\partial_x(\ln \beta)^2 + \partial_y(\ln \beta)^2}$ and $\psi_\beta = \tan^{-1}(\partial_x(\ln \beta)/\partial_y(\ln \beta))$, respectively. Substituting Equation 5 into Equation 2, replacing $|\nabla \tau|$ with $1/c'$, and multiplying both sides by $-c/2$ yields the simplified expression:

$$\alpha - \gamma (\partial_x(\ln \beta) \sin \theta + \partial_y(\ln \beta) \cos \theta) = -\frac{c}{2} \underbrace{\left(2\nabla \tau \cdot \frac{\nabla A}{A} + \nabla^2 \tau \right)}_{\text{apparent attenuation}} \quad (6)$$

where c is estimated from Equation 1 using ASWMS (Jin & Gaherty, 2015) and $\gamma = c/c'$ describes biases due to finite-frequency effects. When finite-frequency effects are small (i.e., $\nabla^2 A / \omega^2 A \approx 0$), structural phase velocity and apparent phase velocity are similar in value and $\gamma \approx 1$, as assumed by previous authors (Bao et al., 2016; Bowden et al., 2017; F. C. Lin et al., 2012). However, we find that $\gamma - 1$ can exceed $\pm 10\%$ (i.e., $\gamma < 0.9$ or > 1.1), particularly at the longest periods (> 130 s). The right-hand side of Equation 6 is referred to as the “apparent attenuation” and is a measured quantity for each earthquake in our data set. The left-hand side of Equation 6 contains the desired structural parameters—attenuation and site amplification—common to all events. To solve for attenuation and amplification, the observations on the right-hand side are fit to a sinusoidal curve as a function of azimuth; the static offset of the sinusoid relates to α , while the amplitude and phase of the azimuthally varying part are related to β (Figure 2).

Maps of apparent attenuation are estimated on an evenly spaced grid with pixel dimensions $0.5^\circ \times 0.5^\circ$. We use γ as an additional quality control parameter, removing pixels for a given event in which $\gamma < 0.9$ or > 1.1 in order to ensure that only the highest quality measurements are considered. For our data set, this threshold is exceeded only at the very longest periods for a small fraction of pixels. For example, only $\sim 8\%$ of pixels are discarded at

130 s period and $\sim 18\%$ are removed at 150 s period. We also discard pixels for a given event with a measured propagation azimuth $> 10^\circ$ from the great-circle path.

Least-squares inversion of Equation 6 yields log amplification gradients, $\partial_x(\ln \beta)$ and $\partial_y(\ln \beta)$, and attenuation coefficient, α , at a given pixel. In practice, it is rare that a single pixel provides a sufficient number of measurements to robustly resolve attenuation and site amplification, and therefore, data from nearby pixels can be grouped together to increase the number of measurements available for inversion. This results in maps that are inherently smoothed by a length proportional to the grouped region. In other words, there is a tradeoff between map robustness (grouping more pixels) and sharpness of lateral variations (grouping fewer pixels). To ensure smooth, well constrained maps, we adopt a binning approach whereby data within 1.5° of a central pixel are gathered and binned within 20° non-overlapping azimuthal bins. The inverse standard deviation of measurements within each azimuthal bin is used to weight the least squares inversion. This procedure is repeated across the study region, producing smoothed 2-D maps of $\partial_x(\ln \beta)$, $\partial_y(\ln \beta)$, and α . In practice, we do not interpret 2-D variations in attenuation due to the small array geometries and uneven azimuthal coverage, and instead, we solve for an array-averaged α by gathering measurements from all pixels within the array and performing a single inversion.

The resulting maps of $\partial_x(\ln \beta)$ and $\partial_y(\ln \beta)$ are used to invert for $\ln \beta$ via the centered 2-D finite-difference formula. The approximate derivatives of log amplification at pixel (x_0, y_0) are given by

$$\partial_x(\ln \beta)|_{(x_0, y_0)} = \frac{\ln \beta_{(x_0+1, y_0)} - \ln \beta_{(x_0-1, y_0)}}{2\Delta_x} \quad (7)$$

$$\partial_y(\ln \beta)|_{(x_0, y_0)} = \frac{\ln \beta_{(x_0, y_0+1)} - \ln \beta_{(x_0, y_0-1)}}{2\Delta_y} \quad (8)$$

where Δ_x and Δ_y is the grid spacing in the x and y directions. The least-squares inversion of Equations 7 and 8 is unable to recover absolute amplification, and instead, we solve for the relative amplification by requiring that the mean of all $(\ln \beta)$ values within the study region is zero. This is equivalent to ensuring that the average β is equal to one. Additional smoothing is imposed on $\ln \beta$ maps by requiring small second spatial derivatives, $\nabla^2(\ln \beta) \approx 0$.

3.3. Constructing the Gradient and Laplacian Fields

The gradient and Laplacian fields of amplitude and phase travel time are required to construct the apparent attenuation term and solve Equation 6 for the attenuation coefficient and local site amplification. One approach for estimating these fields for a given earthquake is to first fit smooth surfaces to absolute phase and amplitude measurements recorded at individual stations and then calculate the spatial gradients of these surfaces using finite-difference operators (Chevrot & Lehujeur, 2022; F.-C. Lin & Ritzwoller, 2011; F.-C. Lin et al., 2009). Removal of outliers is an important step prior to the surface fitting procedure to avoid anomalies in the surface that can amplify upon differentiation. This point is especially crucial for the Laplacian, which requires twice differentiation. Various fitting and regularization approaches have been used such as minimum curvature surface fitting (Bao et al., 2016; F.-C. Lin & Ritzwoller, 2011; F.-C. Lin et al., 2009), smoothing splines, and splines in tension (Chevrot & Lehujeur, 2022). Each approach aims to regularize the interpolation procedure such that gradients are well behaved. While minimum curvature smoothing may be acceptable for Eikonal tomography (Chevrot & Lehujeur, 2022), this form of regularization tends to suppress the Laplacian fields required for Helmholtz tomography, limiting one's ability to account for finite-frequency ($\nabla^2 A$) and focusing/defocusing ($\nabla^2 \tau$) effects.

We adopt an alternative approach for dealing with these challenges; our main philosophy is to avoid applying direct numerical differentiation when possible. We adopt the ray tomography method of Jin and Gaherty (2015), which uses the many interstation travel-time measurements that were determined by cross-correlation to construct the phase slowness vector field, $\nabla \tau$, directly. Below, we show how this can also be extended to the amplitude field to solve for $\nabla A/A$. This approach is attractive for several reasons. First, it does not require fitting a surface to single-station observations, but instead makes use of many more interstation observations derived from cross-correlations and therefore should be less susceptible to noise from any individual measurement. Second, the gradient field is solved for directly meaning that its character (smoothness, curvature) can be easily controlled

via constraint equations within the inversion. Third, only one derivative is needed to calculate the Laplacian field, versus two when surface-fitting is applied to single-station travel-time or amplitude measurements. Finally, formal uncertainties from the inversion procedure are propagated through each step to ensure the best quality measurements are being fit in Equation 6 (see Text S1 in Supporting Information S1 for error propagation equations). We find that this ray-tomography approach more reliably recovers input synthetic attenuation values compared to the surface fitting procedure in some cases (Figure S5 in Supporting Information S1).

The differential phase travel time between two stations i and j , $\delta\tau_{ij}$, is expressed as the path integral of the travel-time gradient (or phase slowness) along the great-circle path connecting the stations. In practice, this equation is discretized, and we solve separately for the x and y components of the travel-time gradient:

$$\delta\tau_{ij} = \int_i^j \nabla\tau \cdot dr \approx \sum_{k=i}^j \partial_x\tau_k \cdot dx_k + \partial_y\tau_k \cdot dy_k \quad (9)$$

where dx_k is the path length through the k th cell projected onto the x -direction with an equivalent definition for dy_k . After solving for the x and y components of the travel-time gradient, apparent phase velocity maps are calculated from $c' = [(\partial_x\tau)^2 + (\partial_y\tau)^2]^{-1/2}$, and the focusing corrections are given by $\nabla^2\tau = \partial_x(\partial_x\tau) + \partial_y(\partial_y\tau)$. We perform an analogous inversion of group travel-times, $\delta\tau_{ij}^g$, for maps of group velocity C , allowing for the estimation of Rayleigh wave attenuation via $Q^{-1} = 2C\alpha/\omega$.

The inverse problem for the x and y components of the gradient field is solved using a least-squares approach with a second derivative smoothing (i.e., minimum curvature) constraint (Jin & Gaherty, 2015). The smoothing operator is rotated to the local radial and transverse directions at each grid cell (assuming great-circle propagation from the earthquake) and a solution is found that minimizes the following penalty function:

$$E = \sum \left| \delta\tau_{ij} - \int_i^j \nabla\tau \cdot dr \right|^2 + \frac{\epsilon\lambda}{\Delta} \sum \left\{ |\nabla^2(\partial_R\tau)|^2 + |\nabla^2(\partial_T\tau)|^2 \right\} \quad (10)$$

where $\partial_R\tau$ and $\partial_T\tau$ are the phase slowness parallel and perpendicular to the great-circle path, respectively. The first sum is over all inter-station travel times, and the second sum is over all grid cells. To impose frequency-dependent smoothing, we weight the smoothing constraint by the ratio of approximate wavelength-to-grid spacing, λ/Δ . The global smoothing parameter, ϵ , is used to balance the relative importance of data fit and model roughness, and we choose a moderate value of 0.1. For our chosen grid spacing of $0.5^\circ \times 0.5^\circ$, this results in overall smoothing weights that range from 0.14 at a period of 20s to 1.1 at 150 s.

Because we solve for the gradient field directly, the second derivative smoothing constraint in Equation 10 is equivalent to minimizing the third spatial derivative of travel time, $\nabla^3\tau$. This requires that the Laplacian field of travel time smoothly varies. While this may limit our ability to resolve sharp gradients in the focusing term, $\nabla^2\tau$, it provides a robust solution given the finite set of unevenly distributed observations. We choose not to apply a first derivative smoothing constraint in the inversion as this would enforce propagation along a great-circle arc, resulting in a focusing correction term that perfectly captures the effects of geometrical spreading, $\nabla^2\tau_{GS}$, but does not account for elastic focusing and defocusing due to lateral velocity gradients.

We use an analogous approach to solve for the normalized amplitude gradient field $\nabla A/A$ found in Equation 6. Because our amplitude measurements are single-station values, we first form the log amplitude difference between a pair of stations, $\delta\ln A_{ij} = \ln A_i - \ln A_j$, and then relate it to the x and y components of the gradient field using

$$\delta\ln A_{ij} = \int_i^j \frac{\nabla A}{A} \cdot dr \approx \sum_{k=i}^j \frac{\partial_x A_k}{A_k} \cdot dx_k + \frac{\partial_y A_k}{A_k} \cdot dy_k \quad (11)$$

This expression is inverted via least squares by minimizing the penalty function analogous to Equation 10. With maps of $(\partial_x A/A, \partial_y A/A)$ and $(\partial_x\tau, \partial_y\tau)$ for each earthquake, we calculate the amplitude gradient along the direction of propagation, $\nabla\tau \cdot \nabla A/A$, and construct the apparent attenuation term (i.e., the right-hand side of Equation 6) and solve for α and β following Section 3.2.

4. Synthetic Wavefield Simulations

Here, we describe realistic wavefield simulations that are used, in Section 5, to evaluate how well attenuation and local site amplification can be recovered from typical OBS array geometries. While the Helmholtz technique has been successfully applied at the USArray for measuring Rayleigh wave attenuation and site amplification (Bao et al., 2016; F. C. Lin et al., 2012), the technique has not yet been applied at an OBS array. In contrast to USArray's uniform ~70 km station spacing, a typical OBS experiment comprises a smaller footprint with often uneven station coverage due to chosen experiment geometry and/or data loss, making it more difficult to accurately recover the gradient and Laplacian fields. Experiments near the continental shelf, such as JdF, represent an especially challenging setting as strong focusing and amplification are expected to occur due to the abrupt velocity contrast at the ocean-continent transition. Additionally, conditions on the seafloor are often noisier than on land, affecting the quality of travel-time and amplitude measurements. Each of these factors contributes to difficulties associated with measuring intrinsic Rayleigh wave attenuation in the ocean basins. To test some of these limitations and validate the approach, we apply the methodology outlined in Section 3 to a realistic synthetic data set comprising the real station and event geometries. This also provides an opportunity to compare the Helmholtz approach with the TPW approach (Forsyth & Li, 2005; Yang & Forsyth, 2006), which has been used to measure attenuation at several OBS arrays (e.g., Ruan et al., 2018; Yang & Forsyth, 2006), in a self-consistent manner.

We generate synthetic seismograms for all of the same events and stations used in the real data set for both the NoMelt and JdF experiments using the SPECFEM3D GLOBE software (Komatitsch & Tromp, 2002a, 2002b). This includes simulations for 160 earthquakes for JdF and 191 at NoMelt. The 3-D elastic model used for the simulations consists of CRUST2.0 (Bassin et al., 2000) overlying the mantle model S362ANI (Kustowski et al., 2008), and attenuation is specified by 1-D model QL6 (Durek & Ekström, 1996). Hereafter, we refer to the full 3-D model as S362ANI + CRUST2.0. The mesh is constructed such that 832 spectral elements lie along the circumference of the Earth, resulting in an average spectral element width of ~48 km and a minimum resolved period of ~20 s.

The synthetic seismograms include realistic effects on Rayleigh wave phase and amplitude caused by wavefield focusing, defocusing, and scattering due to 3-D elastic heterogeneity, intrinsic attenuation, local site amplification, finite-frequency effects, and overtone interference. In addition to calculating seismograms at the true station locations, we also sample the wavefield on an evenly spaced $0.5^\circ \times 0.5^\circ$ grid over a broader region centered on each array (black points in Figure 3). This idealized geometry should allow us to more accurately recover the true gradient and Laplacian fields, providing a benchmark for assessing how well those fields are estimated using the true station geometries. The procedures used to measure phase and amplitude and invert for gradient and Laplacian fields for the synthetic data set are identical to those used for the real data.

NoMelt and JdF represent endmember locations in terms of structural complexity. Figure 3 shows phase velocity maps at 31 and 84 s period for S362ANI + CRUST2.0, which were calculated by sampling 1-D profiles from the 3-D model at 1° intervals and applying MINEOS to calculate Rayleigh wave dispersion. The maps have been corrected for the effect of physical dispersion using a reference frequency of 1 Hz (H. Liu et al., 1976). Although the wavefield simulations are performed on a fully 3-D model, these phase velocity maps are a useful representation of the structure sampled by Rayleigh waves of a certain period. There is a clear contrast between NoMelt and JdF, particularly at 31 s period, for which phase velocities vary by more than $\pm 2\%$ at JdF but are typically $<0.5\%$ at NoMelt. We note that slow velocities associated with the JdF Ridge (e.g., Bell et al., 2016) are absent from the coarse 3-D model. Regardless, the sharp velocity contrast associated with the continent-ocean transition still allows us to test the limitations of the methodology.

In order to avoid confusion, we define terminology to clearly distinguish between quantities derived from the real data set and those derived from the synthetic simulations. Hereafter, we refer to the synthetic waveforms and measurements derived from them as “synthetics” and the real observations as the “data.” In addition, “measurements” are any quantities estimated from Helmholtz tomography (i.e., Equations 1–11) and can apply to data or synthetics, and “predictions” refer to synthetic calculations of a given quantity from the S362ANI + CRUST2.0 model (i.e., using MINEOS). These predictions are useful because they represent the target for recovery in our synthetic tests. By comparing the synthetic measurements to these predictions, we can explore limitations of the methodology related to station coverage and/or wavefield complexities.

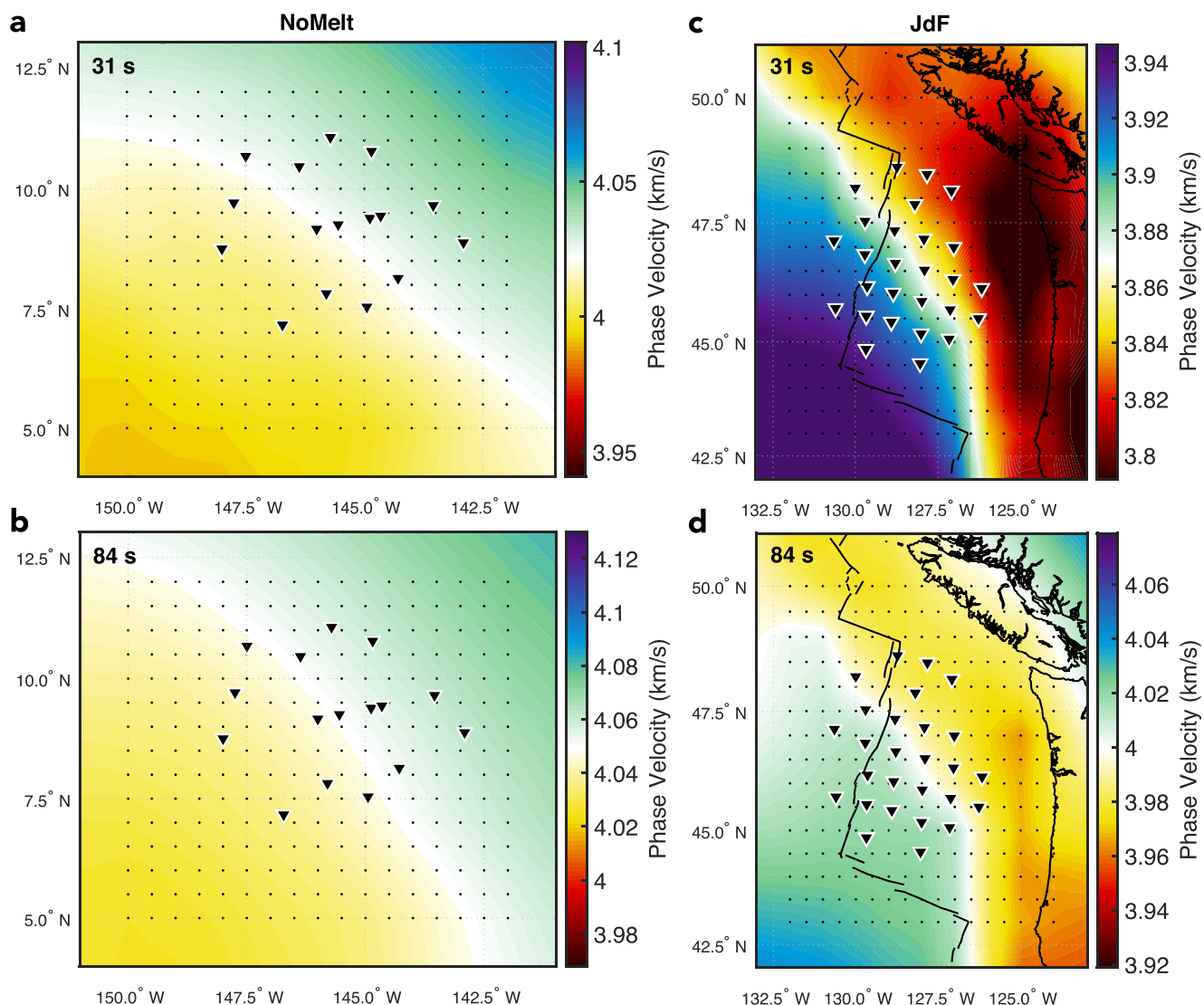


Figure 3. Predicted synthetic Rayleigh wave phase velocity maps for 3-D global mantle model S362ANI (Kustowski et al., 2008) combined with CRUST2.0 (Bassin et al., 2000) at (a and c) 31 s and (b and d) 84 s period. Maps are predicted by sampling 1-D profiles every 1° from the 3-D model and calculating dispersion using MINEOS. (Left) NoMelt and (right) Juan de Fuca station geometries are indicated by black triangles. The finely spaced ($0.5^{\circ} \times 0.5^{\circ}$) black points show the locations at which the SPECFEM3D GLOBE synthetic wavefield was sampled for idealized synthetic testing in Figures 4a–4c; this sampling interval is approximately equal to one spectral element and corresponds to the grid spacing used in the ray tomographic inversion for the gradient fields. Colors range from -2% to $+2\%$ about the mean velocity. Maps are corrected for physical dispersion using the 1-D model QL6 (Durek & Ekström, 1996) and a reference frequency of 1 Hz.

5. Results

In the following sections, we present the results of applying Equation 6 to both synthetics and real data at NoMelt and JdF. Synthetics are treated identically to the data throughout the analysis. First, we demonstrate the ability to faithfully recover the focusing correction term ($\nabla^2 \tau$) and compare this term for the two study sites (Section 5.1). We then present maps of site amplification (β) for both data and synthetic at both locations and demonstrate that the measured synthetic maps match theoretical predictions (Section 5.2). Array-averaged estimates of attenuation (α) are then presented for both data and synthetic, and comparisons are made with the TPW technique (Section 5.3). Finally, we invert array-averaged attenuation for 1-D profiles of shear attenuation (Q_μ^{-1}) at NoMelt and JdF and compare our results with previous studies (Section 5.4).

5.1. Focusing Corrections

Figure 4 shows example maps of apparent amplitude decay, focusing correction, and corrected amplitude decay for a M_w 6.4 earthquake originating at the southern East Pacific Rise and propagating north-northwest across the JdF array. The propagation direction approximately parallels the coastline, representing an extreme case of focusing and defocusing that manifests as strong NW-SE banding that is parallel to the direction of wave propagation in the amplitude decay maps (Figures 4a, 4d and 4g). Three main observations can be made: First, the focusing effects are significant and greatly impact the amplitude decay field (Figures 4a–4c). Second, the true station geometry is sufficient for resolving the focusing correction term and, in turn, the corrected amplitude decay field (Figures 4d–4f). Third, the data show a similar overall behavior to the synthetic measurements, indicating that even in the noisy seafloor environment focusing effects can be observed and corrected for (Figures 4g–4i).

The amplitude decay (Figures 4a, 4d and 4g) and focusing correction terms (Figures 4b, 4e and 4h) display similar patterns that are opposite in sign such that the coastline-parallel banding is significantly reduced when added together to form the corrected amplitude decay map (Figures 4c, 4f and 4i). For this event, the sign of the strongest focusing correction is positive (blue) indicating *defocusing* of the wavefield. In other words, wave amplitudes in the blue regions of Figures 4b, 4e and 4h decay more strongly than dictated by intrinsic attenuation, and thus, failing to correct for defocusing would result in attenuation estimates that are biased high at those pixels for this event. In contrast, the region of strong amplitude decay (red) near the coastline in Figure 4a is not removed by the focusing correction and therefore is likely related to site deamplification at the coastline. The slightly positive regions at the edges of the corrected amplitude decay maps (Figures 4f and 4i) are likely artifacts due to edge effects in the gradient and/or Laplacian estimates. Because we consider many events from various azimuths, such edge effects do not strongly bias estimates of attenuation or site amplification.

The resemblance between the synthetic and observed focusing corrections in Figure 4 is remarkable given the high noise levels typically associated with OBS data and suggests that the velocity structure of S362ANI + CRUST2.0 between this particular source on the East Pacific Rise and JdF receivers (see Figure S1 in Supporting Information S1) resembles the true structure at 55 s period. However, the maximum amplitude of the focusing corrections for the real data is larger by a factor of ~5, likely due to the global model being smooth, which reduces the overall amplitude of focusing and defocusing. We note that the synthetic and real gradient fields compare less favorably for propagation paths that are oriented more perpendicular to the coastline (not shown) as the presence of the JdF Ridge has a strong influence on the real data set but is not well resolved by the long-wavelength S362ANI + CRUST2.0 structure.

We further explore the focusing corrections by investigating their distribution for all events in our catalog at both NoMelt and JdF (Figure 5), after removing the effects of geometrical spreading via Equation 4. As discussed in Section 3.1, the resulting structural focusing correction ($\nabla^2 \tilde{r}$) should reflect focusing/defocusing due to lateral variations in wavespeed along the ray path, both prior to the Rayleigh wave entering the array as well as within the array footprint. We speculate that structural variations along the ray path prior to the Rayleigh wave entering the OBS array should more strongly influence the overall focusing/defocusing behavior (e.g., width of the distribution) because the OBS array footprint is relatively small (only ~5° compared to tens of degrees of propagation between earthquake source and the edge of the array). However, strong local velocity gradients within, or nearby, the array will influence the finer details of the focusing patterns (e.g., skew of the distribution).

Overall, we observe that the distributions of focusing corrections at NoMelt are narrow, strongly peaked around zero, and relatively symmetric for both data and synthetic, while at JdF they are more broadly distributed indicating stronger focusing/defocusing. This is consistent with more complicated source-receiver paths and waves that interact with the coastline at JdF as well as the stronger velocity gradients present in the JdF region compared to NoMelt (Figure 3). In detail, the distribution of focusing correction terms at 31 s period is skewed from zero at JdF, and this skew in the real data (Figure 5d) occurs in the opposite sense from the skew in the synthetic measurements (Figure 5a). A negative skew in the data indicates a tendency for the wavefield to be focused upon entering the array, while a positive skew in the synthetics indicates defocusing.

The local velocity structure at JdF is likely one factor that contributes to the different sense of skew for the focusing corrections measured from data and synthetics. Figure 5f shows the phase velocity map estimated from Equation 1 using our dense OBS observations, while Figure 5c shows phase velocity predicted for S362ANI + CRUST2.0 using MINEOS. Perhaps unsurprisingly, phase velocity measured from the real OBS

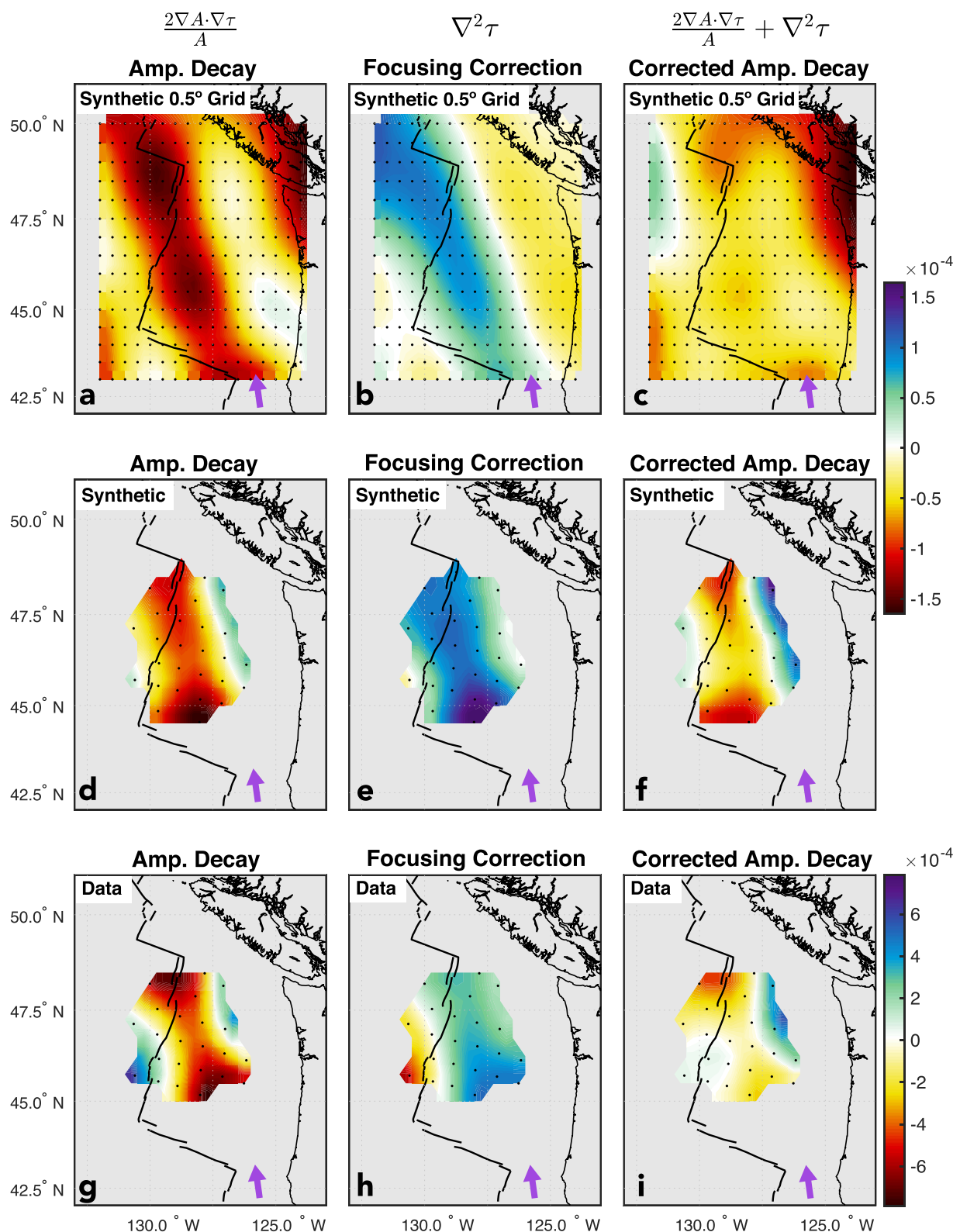


Figure 4. Demonstration of the 55 s period focusing/defocusing correction at Juan de Fuca for a M_w 6.4 strike-slip earthquake that occurred at the southern East Pacific Rise on 12 May 2014 (13:58:21.5 GMT). Measured maps of (a) apparent amplitude decay, (b) focusing correction, and (c) corrected amplitude decay estimated from SPECFEM3D GLOBE synthetics for idealized station spacing of $0.5^\circ \times 0.5^\circ$. Black points indicate station/sampling locations from Figure 3. The purple arrow shows the direction of wave propagation. Panels (d–f) same as panels (a–c), but measured from SPECFEM3D GLOBE synthetics sampled at the true ocean-bottom seismometer locations. Panels (g–i) same as panels (d–f), but measured from the real data. Note the larger range of values in panels (g–i).

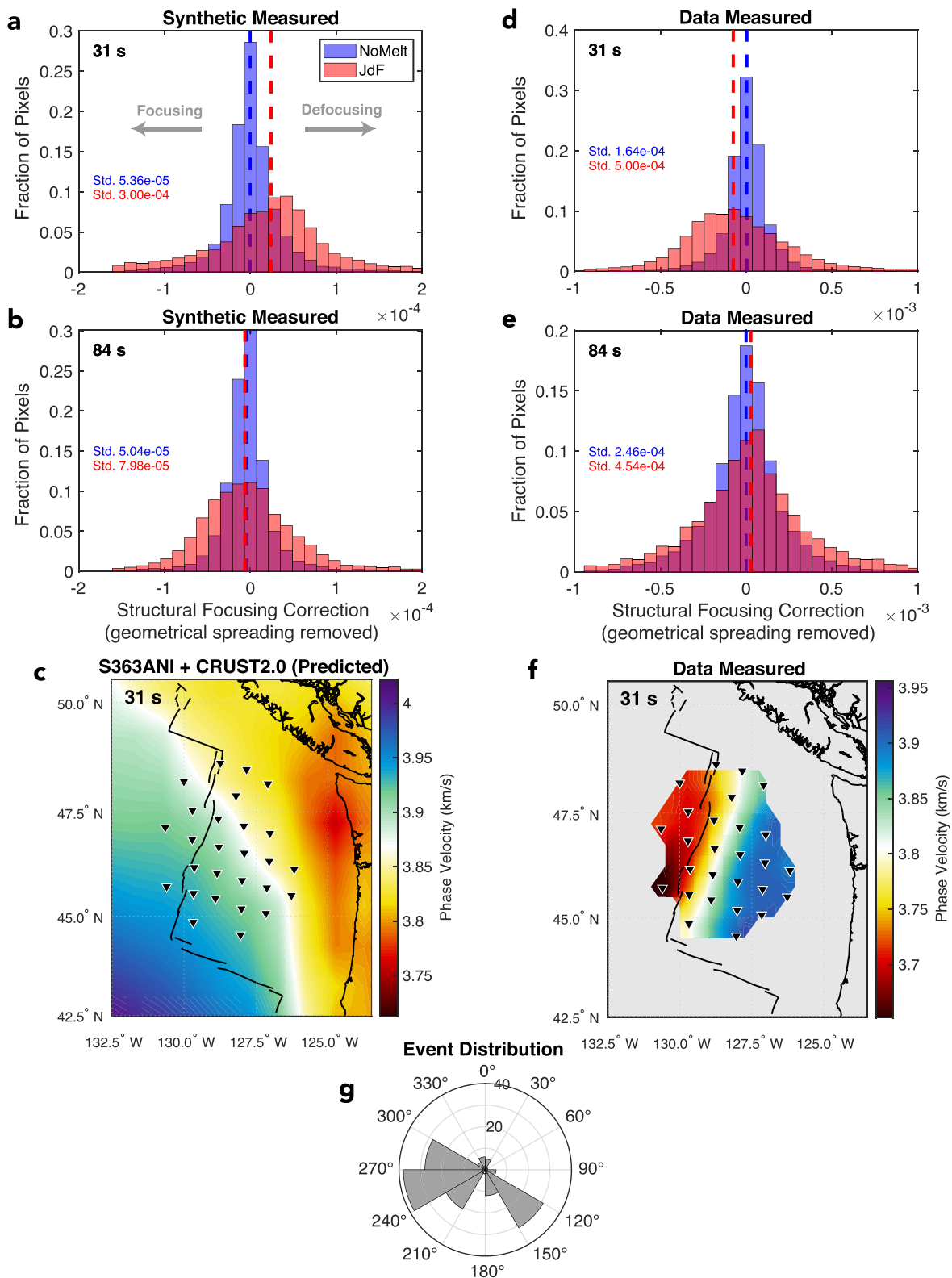


Figure 5.

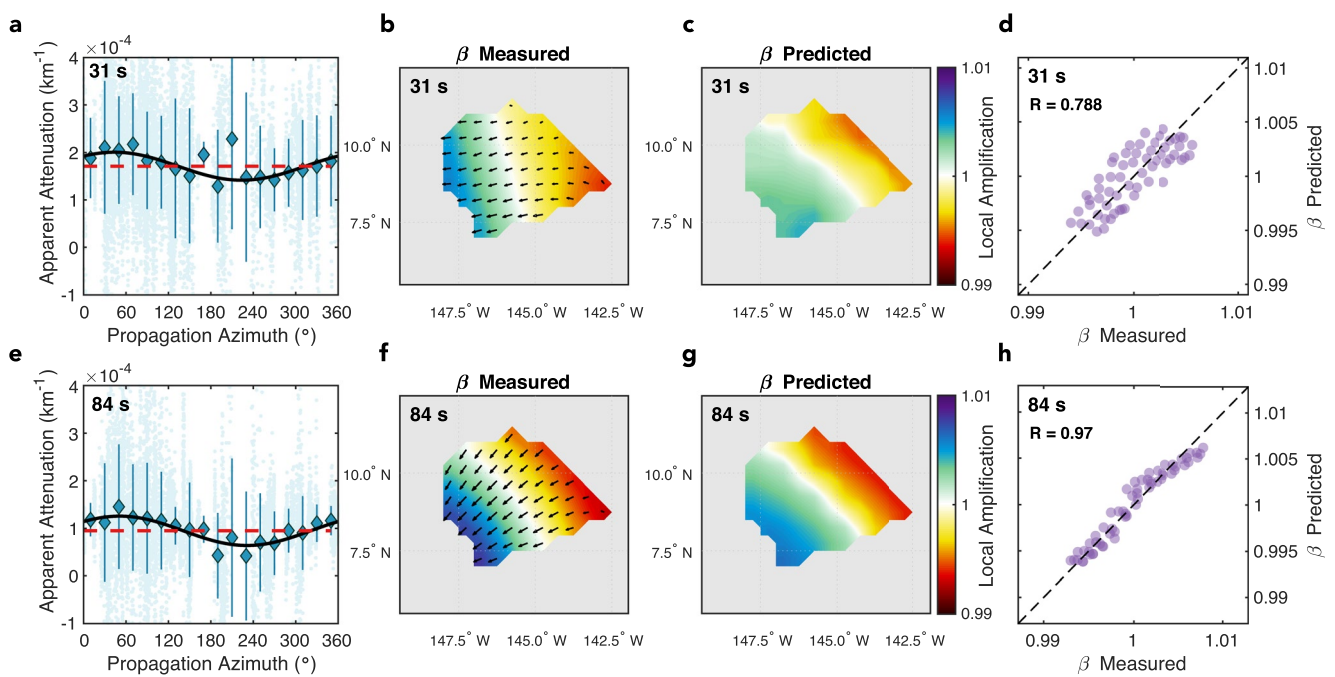


Figure 6. Synthetic recovery test of site amplification, β , at NoMelt. (a) Measurements of array-averaged apparent attenuation (i.e., right-hand side of Equation 6) at 31 s period for all events and pixels. Blue diamonds and error bars show the mean and standard deviation of points within 20° azimuthal bins, and the best fitting 1-D sinusoid is shown in black. The red dashed line indicates the estimate of array-averaged anelastic attenuation, α . To estimate lateral variations in amplification, we apply this same fitting procedure pixel-by-pixel (see Section 3.2 for details). (b) Measured amplification maps via Equations 7 and 8, where black vectors show the log amplification gradient at each pixel obtained by binning measurements within a 1.5° radius and performing fitting as in panel (a). (c) Amplification predicted from the 3-D synthetic model S362ANI + CRUST2.0 using Equations 12 and 13. (d) Comparison of measured and predicted amplification with correlation coefficient shown at the top left. Panels (e–h) same as panels (a–d), but for 84 s period. Both measured and predicted amplification maps are normalized such that the average within the array equals 1. Values of $\beta > 1$ correspond to relative amplification and $\beta < 1$ correspond to relative deamplification.

data provides sharper constraints on the low velocity JdF Ridge than does S362ANI, which was developed using basin-traversing surface waves and body waves recorded at land stations (Kustowski et al., 2008). The presence of the low-velocity JdF Ridge (<3.7 km/s at 31 s period) along the western edge of the array, together with the strongly biased event distribution (Figure 5g) with most events arriving from the west, has a measurable impact on the focusing correction terms. Waves entering the array from the west in the real Earth are preferentially focused by the slow velocities along the JdF Ridge, while waves from those same events in the synthetic model are defocused by the fast oceanic plate velocities to the west. Again, the focusing corrections for the real data are 4–5 times larger than for the synthetics, likely due to the smoothness of the synthetic model. Regardless of the absence of the JdF Ridge in the synthetic model, the abrupt velocity contrast associated with the ocean-continent transition still offers a useful scenario for testing the limitations of Helmholtz tomography in the presence of strong elastic focusing.

5.2. Local Site Amplification

Before estimating local amplification from real data, we first use the synthetic travel time and amplitude measurements to explore how well it can be recovered (Figures 6 and 7) using the realistic event and OBS array

Figure 5. Distribution of structural focusing corrections, $\nabla^2\tilde{\tau}$, at NoMelt (blue) and Juan de Fuca (JdF) (red) at (a) 31 s and (b) 84 s period measured from the synthetics using the true station geometries (left) and measurements from the real data (right). The effect of geometrical spreading has been removed via Equation 4, and therefore wave focusing (negative values) and defocusing (positive values) are due to lateral variations in wavespeed along the propagation path. Vertical dashed lines show the median values of the distributions. (c) Synthetic phase velocity map at 31 s period, predicted using MINEOS as in Figure 3. Panels (d–f) same as panels (a–c), but for the real data. The measured phase velocity map in panel (f) was produced by solving Equation 1 and stacking over all events following Jin and Gaherty (2015). (g) Distribution of earthquake back azimuths at JdF, indicating most events originate from the west. Focusing behavior for data and synthetic is similar overall, except for at JdF at 31 s period, where the skew in correction terms for the real data indicates preferential focusing. This difference arises from the slow velocities along the western edge of the array associated with the JdF Ridge (f)—replaced by fast velocities in the synthetic model (c)—which focuses waves arriving from the west. Note the factor of 5 larger horizontal axis range in panels (d and e) compared to panels (a and b).

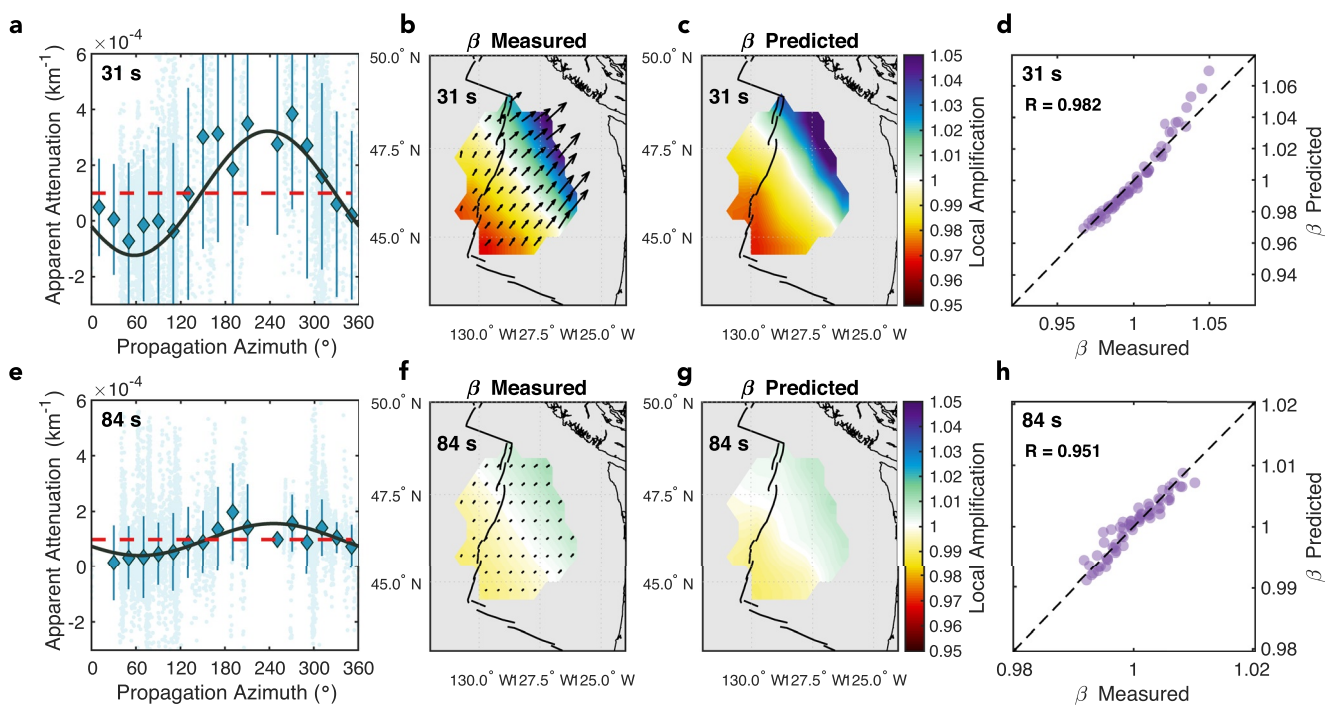


Figure 7. Synthetic recovery test of site amplification, β , at Juan de Fuca. See Figure 6 caption for details.

geometries. Amplification is estimated from the azimuthal variation of apparent attenuation (e.g., Figures 2, 6a and 7a) via Equation 6. The minimum of the sinusoid corresponds to the azimuth of maximum Rayleigh wave amplification, $\beta > 1$ (likewise, the peak of the sinusoid indicates the azimuth of maximum deamplification, $\beta < 1$). For example, Figure 7a shows a minimum at $\sim 60^\circ$ for the synthetic JdF data set, which indicates that waves traveling northeast across the array are preferentially amplified. This is reflected in the maps of β (Figure 7b). In this case, failing to account for amplification would result in an apparent $\alpha < 0$ for observations at this propagation azimuth (i.e., wave amplitudes *increase* with propagation distance). This demonstrates the importance of considering Rayleigh wave amplification and attenuation together as well as the need for decent azimuthal coverage, which is discussed further in Section 6.1.

We compare the amplification measured from synthetics to amplification predicted for the 3-D model S362ANI + CRUST2.0, which we consider ground truth, at a desired pixel and frequency from the following expressions (F. C. Lin et al., 2012)

$$\beta(x, y, \omega) = \left(\frac{cCI}{\overline{cCI}} \right)^{-\frac{1}{2}} \quad (12)$$

$$I = \frac{1}{U(a)^2} \int_0^a \rho(r) (U(r)^2 + V(r)^2) r^2 dr \quad (13)$$

where \overline{cCI} is the average value within the array, therefore ensuring the mean of the predicted β maps equals one as prescribed by the inversion (see Section 3.2), $\rho(r)$ is density at radius r , and U and V are the vertical and horizontal displacement eigenfunctions at position (x, y) , respectively. The integral is carried out from Earth's center to the seafloor at radius a .

Relative amplification (β) is recovered successfully from the synthetics at both NoMelt (Figure 6) and JdF (Figure 7) at periods of 31 and 84 s using the real station geometries and event distributions. The correlation coefficient between measured and predicted values at both locations is >0.95 , except for at NoMelt at 31 s period ($R = 0.788$; Figure 6d) for which amplification and deamplification are weak ($<0.5\%$). Measured and predicted β maps at both locations are roughly anti-correlated with the phase velocity maps shown in Figure 3, as expected

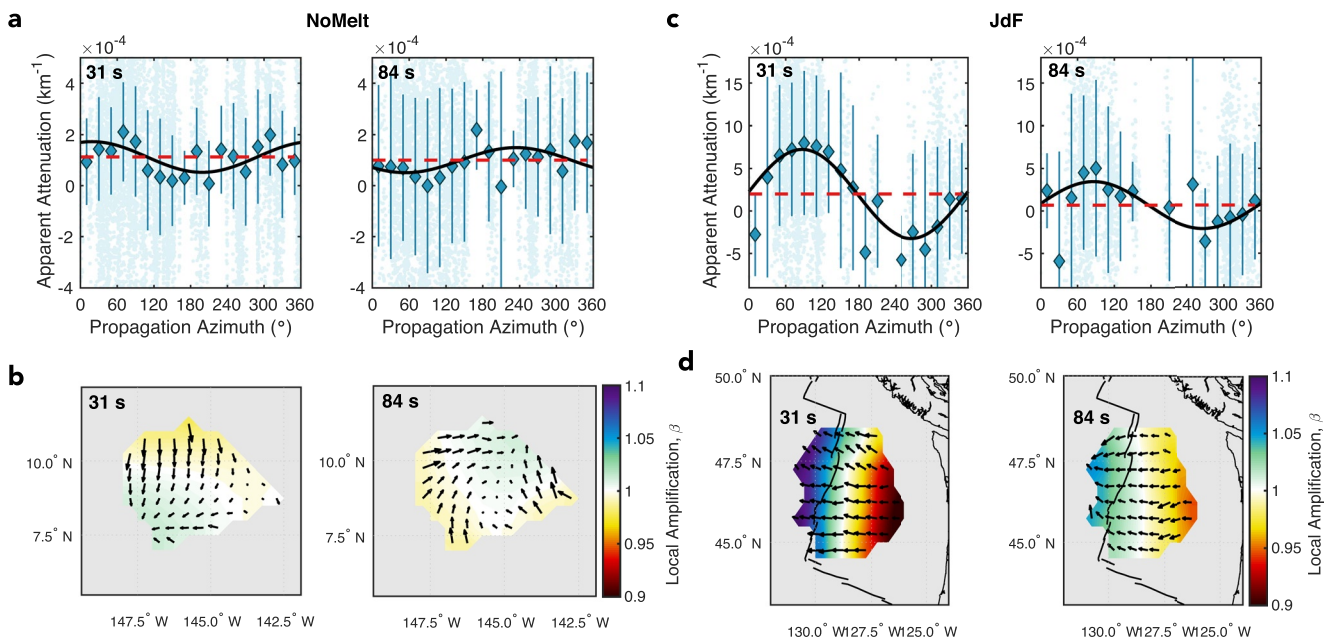


Figure 8. Amplification maps observed from the real data sets. (a) Apparent attenuation measurements (right-hand side of Equation 6) and (b) local amplification maps at NoMelt at 31 and 84 s period. Panels (c and d) same as panels (a and b), but for Juan de Fuca. Symbols as in Figures 6 and 7. Amplification maps are normalized by the array-averaged value. Note the difference in the vertical axes in panels (a and c).

(F. C. Lin et al., 2012). Regions of amplification and deamplification tend to correspond to slow and fast phase velocities, respectively, at least to first order. Amplification at NoMelt varies by <1% due to the relatively modest velocity variations in S362ANI + CRUST2.0 at this location, whereas JdF shows variations of up to 5%–7% amplification at 31 s period due to the strong low velocities on the eastern edge of the array associated with the transition to continental crust.

The highest predicted values of 31 s amplification at JdF of ~1.07 are slightly underestimated by the synthetic measurements at ~1.05 (Figure 7d). This may be due to the strongest amplification in the northeast being located at the edge of the map where fewer measurements are available for binning within the surrounding 1.5° radius for the inversion. On the other hand, strong deamplification values ($\beta < 1$) at the southwest edge of the map are very well recovered. Another possibility is that a slight tradeoff exists between β and α due to the uneven azimuthal coverage (Figure 5g). Although our 20° azimuthal binning procedure should lessen such biases, azimuthal gaps inevitably exist for any given pixel in the map.

Figure 8 shows apparent attenuation and local amplification measured from the real data. The real observations reveal similar first order variations in β as the synthetic measurements and predictions at NoMelt and JdF with overall weak amplification/deamplification at NoMelt (Figures 8a and 8b) and stronger values at JdF (Figures 8c and 8d). The observed amplification variations at NoMelt are less spatially coherent at the two periods of interest, likely because the magnitudes of amplification and deamplification variations at NoMelt are small (<1%); indeed, the synthetic recovery tests demonstrate that weaker amplification variations are more difficult to resolve (Figure 6d). In contrast, β maps at JdF show strong variations in amplification (>10% at 31 s period) that are spatially coherent at both periods of interest and correlate reasonably well with the low-velocity JdF Ridge (Figure 5f). These are among the first amplification maps observed in an oceanic setting and can be used together with complementary observations of Rayleigh wave phase velocity to better constrain shear and compressional velocities and density of the crust and uppermost mantle (e.g., Bowden et al., 2017; F. C. Lin et al., 2012), a future research direction discussed further in Section 6.3.

5.3. Array-Averaged Rayleigh Wave Attenuation

Before estimating Rayleigh wave attenuation from real data, we first use the synthetic measurements to explore how well it can be recovered (Figure 9) using the realistic event and OBS array geometries. In general, we successfully

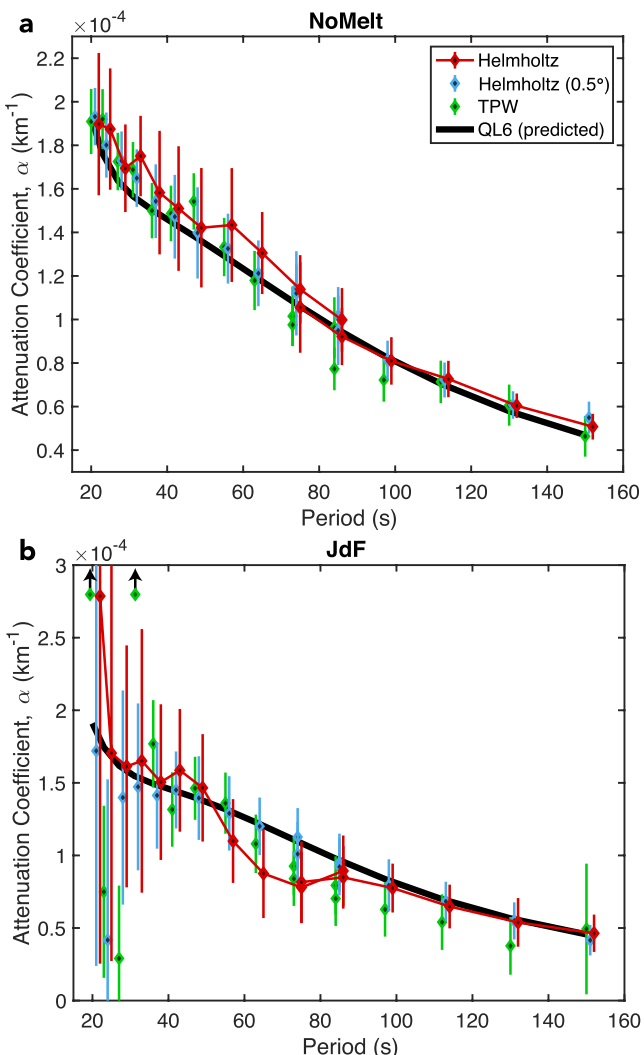


Figure 9. Recovery of synthetic 1-D attenuation coefficient, α , at (a) NoMelt and (b) Juan de Fuca for periods of 20–150 s. The predicted (target) attenuation values of QL6 (Durek & Ekström, 1996) are shown in black. Red symbols show Helmholtz measurements that utilize the true station geometry at each array. For comparison, the Helmholtz measurements for the idealized $0.5^\circ \times 0.5^\circ$ station spacing are shown in blue, and green symbols show measurements from the two-plane wave (TPW) inversion utilizing the phase and amplitude data set for the true station geometry. The upward pointing black arrows at 20 and 31 s indicate TPW measurements that plot beyond the vertical axis bounds ($\alpha \sim 26.9 \times 10^{-4}$ and $4.9 \times 10^{-4} \text{ km}^{-1}$, respectively).

recover the input 1-D Rayleigh wave attenuation at both NoMelt and JdF. To obtain these array-averaged estimates of attenuation at each period, we group together all apparent attenuation measurements for the whole study area (i.e., all events and pixels) and use our curve-fitting approach to solve for a single value of α (and $\nabla\beta/\beta$). Our implicit assumption that a single value of $\nabla\beta/\beta$ at each period can sufficiently represent the true variation in the maps in Figures 6 and 7 is reasonable given that β tends to vary smoothly (and simply) across our small study regions such that its gradient is relatively constant across the region. Violation of this assumption should result in more scatter around the true α value, leading to larger α uncertainties, but should not significantly bias the array-averaged α estimate.

Uncertainties in the recovered α values are generally smaller at NoMelt than JdF likely owing to the weaker focusing and defocusing effects (Figure 5), weaker amplification variations (Figure 6), and better azimuthal coverage (Figure 1). Uncertainties at JdF are especially large for periods <30 –40 s likely due to the assumption of 1-D $\nabla\beta/\beta$ not being completely valid at these periods as indicated by amplification gradients that tend to increase to the northeast (black arrows in Figure 7b). It is also possible that the strong focusing and defocusing at these periods is not perfectly accounted for, even for these noise-free synthetic tests, due to the complex focusing patterns and difficulties resolving $\nabla^2\tau$ with sparse station coverage. Unaccounted for scattering attenuation due to the abrupt velocity changes at the coastline may also contribute to these larger uncertainties. We note that average attenuation is slightly underestimated at JdF at periods of 60–80 s using the true station coverage, but it is well estimated at these periods using the idealized 0.5° station geometry (blue symbols in Figure 9), which suggests that the slight underestimate is related to a lack of station coverage. Nevertheless, Figure 9 shows that the input attenuation values are well recovered (to within uncertainty) at all periods from 20 to 150 s at both locations.

Attenuation recovered from the synthetics using the true station geometry (red symbols in Figure 9) agrees with values recovered from the synthetics using the idealized 0.5° grid (blue symbols), albeit with larger uncertainties. The smaller uncertainties across all periods for the idealized station geometry likely reflect its ability to better recover the true focusing and defocusing corrections. However, for periods <35 s at JdF, uncertainties are larger relative to other periods also for the idealized geometry. This is consistent with the idealized geometry encompassing a broad area (even larger than the true geometry) for which the assumption of 1-D $\nabla\beta/\beta$ is not strictly valid, particularly at these shorter periods. In addition, we cannot rule out that focusing correction terms are not perfectly resolved and could perhaps be improved with finer station spacing ($<0.5^\circ$) and/or a weaker second-derivative smoothing constraint.

We compare our Helmholtz results with those of the TPW inversion (Forsyth & Li, 2005; Yang & Forsyth, 2006) applied to the same synthetic phase and amplitude data set using the true station geometry (green symbols in Figure 9). Because the data sets are identical, differences between the TPW and Helmholtz results are entirely due to differences in the theoretical treatments of phase and amplitude. We find excellent agreement between Helmholtz and TPW at all periods at NoMelt and at periods >40 s at JdF, where focusing and defocusing are relatively weak (Figure 5). For these scenarios, the wavefield can be sufficiently approximated by two interfering plane waves. However, at JdF large differences appear at periods <35 s, where TPW is unable to recover the true 1-D attenuation within uncertainty. This breakdown of the TPW technique indicates that the complex wavefield

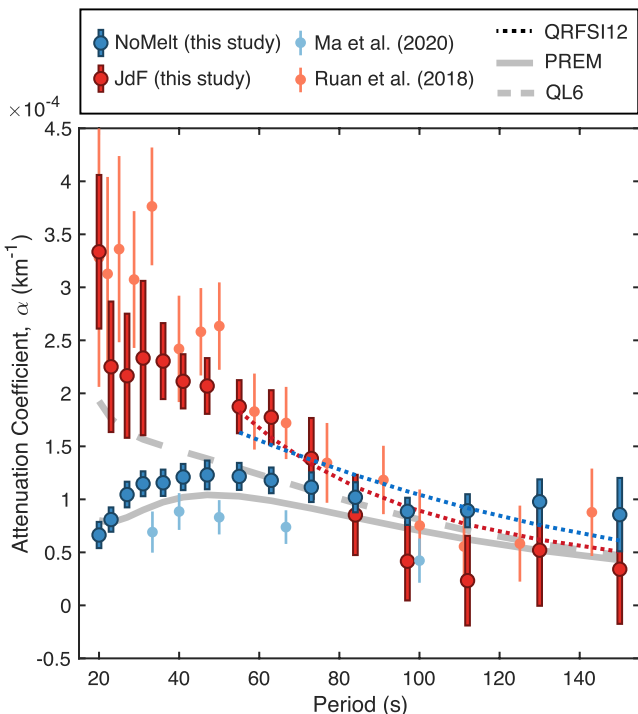


Figure 10. Measured 1-D attenuation coefficients for periods ranging from 20 to 150 s for NoMelt (blue) and Juan de Fuca (JdF) (red). For comparison, two-plane wave derived measurements from two previous studies are shown for NoMelt (Ma et al., 2020) and JdF (Ruan et al., 2018). 1-D global models QL6 (Durek & Ekström, 1996) and PREM (Dziewonski & Anderson, 1981) are shown in gray. Dotted lines show attenuation from the 3-D global model QRFSI12 (Dalton et al., 2008) estimated at the center of each deployment location using MINEOS. Error bars represent 2σ uncertainty.

in μ and κ , respectively. Since both upper-mantle bulk attenuation and the sensitivity of Rayleigh waves to it are much smaller than is the case for shear attenuation, we fix Q_κ^{-1} to PREM values (Dziewonski & Anderson, 1981). We perform a regularized least-squares inversion of Equation 14 for Q_μ^{-1} in the depth range 0–450 km with norm damping and second derivative smoothing, using MINEOS to calculate the sensitivity kernels (see Figure S4 in Supporting Information S1). The sensitivity kernels primarily depend on the shear velocity structure, and therefore we first invert average phase velocity dispersion data for a smooth 1-D shear velocity profile at each location. We then invert for Q_μ^{-1} using the two-layer NoMelt attenuation model of Ma et al. (2020) as the starting model for both NoMelt and JdF, adjusting the water depth accordingly, but do not find a strong dependence on assumed starting attenuation model. Crustal Q_μ is held fixed at 1,400. Model uncertainties are estimated through a bootstrap resampling approach in which the attenuation data are randomly perturbed within their uncertainty bounds and reinverted. This is repeated 500 times producing an ensemble of models, and the 1σ uncertainties are estimated from the middle 68% of the ensemble.

The resulting 1-D models of shear attenuation and their fit to the data are shown in Figure 11. Shear attenuation at NoMelt is characterized by a low attenuation lithospheric layer ($Q_\mu > 1,500$) overlying a high attenuation asthenospheric layer ($Q_\mu \sim 50$ to 70) with a transition between the two occurring from ~50 to 100 km depth. At JdF, we observe a broad peak in attenuation ($Q_\mu \sim 50$ to 60) centered at a depth of 100–130 km, bounded above and below by low attenuation regions ($Q_\mu > 200$). In both cases, uncertainties increase with depth due to the larger uncertainties at longer periods.

focusing and defocusing near the coastline in the S362ANI + CRUST2.0 model cannot be sufficiently described by the interference of two plane waves.

The 1-D attenuation coefficients measured from the real data sets are presented in Figure 10 for NoMelt (blue) and JdF (red). Attenuation is higher at JdF than NoMelt for periods <70 s, whereas the opposite is true for periods >90 s. To first order, our new observations at the two regions compare favorably with previous measurements using the TPW technique (lighter colored symbols in Figure 10), but important differences exist. Our observations show higher attenuation at all periods at NoMelt and slightly lower attenuation on average at most periods at JdF. Attenuation at NoMelt is slightly higher than PREM values at all periods >30 s, whereas JdF shows much higher attenuation than PREM at periods <80 s and comparable attenuation at periods >80 s. Attenuation from global model QRFSI12 (Dalton & Ekström, 2006; Dalton et al., 2008) sampled within the NoMelt and JdF regions is roughly consistent with our new measurements at >50 s period, but we find bigger differences in attenuation between the two regions than QRFSI12.

5.4. Shear Attenuation Profiles

We invert our new Helmholtz measurements of Rayleigh wave attenuation for profiles of upper mantle shear attenuation at NoMelt and JdF (Figure 11). Frequency-dependent Rayleigh wave attenuation, $Q^{-1}(\omega)$, is related to shear attenuation, $Q_\mu^{-1}(r)$, and bulk attenuation, $Q_\kappa^{-1}(r)$, as a function of radius r through the expression (Dziewonski & Anderson, 1981)

$$Q^{-1}(\omega) = \int_0^a [\mu(r)K_\mu(\omega, r)Q_\mu^{-1}(r) + \kappa(r)K_\kappa(\omega, r)Q_\kappa^{-1}(r)] dr \quad (14)$$

where μ and κ are the shear and bulk moduli, respectively, and K_μ and K_κ are the Fréchet kernels describing sensitivity of Rayleigh waves to changes

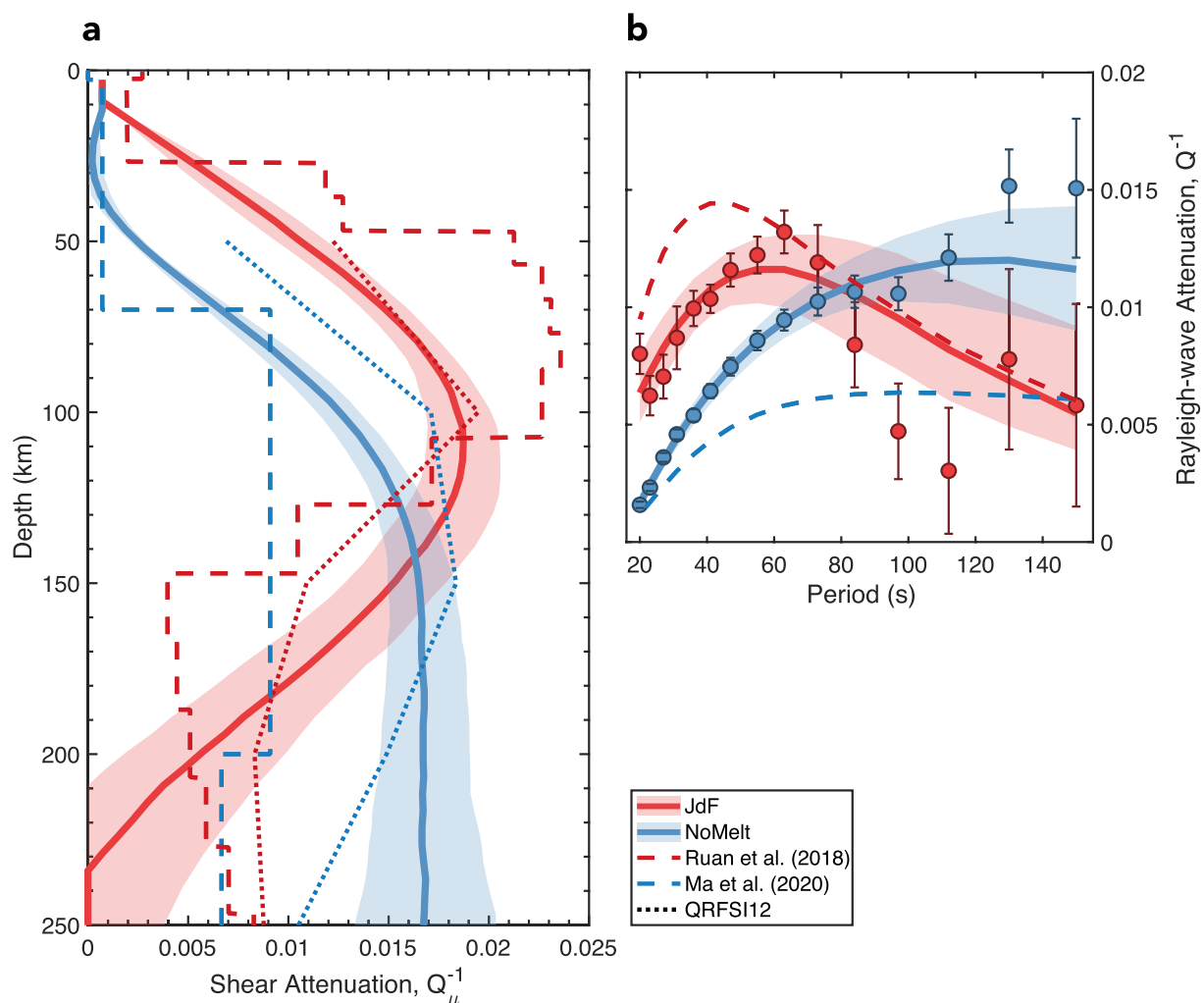


Figure 11. (a) Inversion for 1-D shear attenuation profiles at NoMelt (blue) and Juan de Fuca (JdF) (red). The solid lines and shaded regions show the median and 68% confidence interval, respectively, from bootstrap resampling. (b) Model fit to our data (filled circles with 1σ error bars). Previous 1-D shear attenuation models and predictions for NoMelt (Ma et al., 2020) and JdF (Ruan et al., 2018) are shown by dashed lines. Dotted lines show attenuation profiles from global model QRFSI12 (Dalton et al., 2008) extracted from the approximate deployment locations.

6. Discussion

6.1. Advantages and Limitations of Helmholtz Tomography

We demonstrate that Helmholtz tomography can recover 1-D Rayleigh wave attenuation and 2-D maps of site amplification using typical OBS array geometries, even in the presence of strong elastic focusing and defocusing due to coastline effects. The power of the approach lies in its ability to account for complex patterns of elastic focusing without imposing strict physical assumptions about the nature of wavefield interference. Rather, the focusing behavior is directly observed and accounted for via $\nabla^2\tau$. In contrast, the TPW approach imposes a physical limitation on wavefield complexity. This approximation is sufficient in many settings, such as structurally homogeneous regions of the ocean basins far away from continents, like NoMelt, but it may break down in more complex areas such as JdF, where the coastline has a large influence on multipathing behavior at periods <35 s (Figure 9b). On the other hand, an important limitation of Helmholtz tomography is that it requires decent station coverage in two dimensions in order to accurately resolve the gradient and Laplacian fields in Equation 6. Sharp lateral variations in these fields are challenging to resolve given the smooth regularization scheme used (Equation 10) and/or limitations in station coverage. In situations where station coverage is lacking, the TPW approach may be advantageous as the assumption of two interfering plane waves provides a solid physical basis for extrapolating wavefield behavior across data-poor regions.

Helmholtz tomography is able to simultaneously account for both attenuation and site amplification via the mean and azimuthal variation of apparent amplitude decay, respectively. Accounting for local site amplification when estimating attenuation is especially important if amplification variations are strong and/or azimuthal gaps exist in the data set. Both sources of bias can be understood by considering the synthetic JdF data set as an example (Figures 7a and 7e). Apparent attenuation varies strongly with azimuth, especially at 31 s, and thus a data set dominated by waves that propagate to the northeast at 60° azimuth would lead to attenuation estimates at JdF that are biased low (negative even), whereas the opposite would be true of a data set dominated by waves propagating to the southwest at 240°. Such biases will increase with the magnitude of amplification variations (compare Figures 7a and 7e). Therefore, a decent azimuthal distribution of teleseismic earthquakes is necessary to prevent tradeoffs between attenuation and site amplification, especially if amplification variations are strong.

In this study, we focus on characterizing the average Rayleigh wave attenuation within small seismic arrays. Solving for 2-D maps of Rayleigh wave attenuation is desirable but challenging due to the issues outlined above, such as limited station coverage and potential tradeoffs due to uneven azimuthal distribution of earthquakes. Indeed, previous studies that utilized data from the USArray encountered challenges resolving detailed 2-D attenuation maps (F. C. Lin et al., 2012) and required both masking and spatial smoothing up to ~3° radius (Bao et al., 2016). Such smoothing would effectively smear away any lateral variation within a typical OBS array on the order of ~500 km × 500 km. We therefore focus on 1-D array-average estimates of attenuation. As OBS arrays are typically small, 1-D attenuation is useful for characterizing OBS deployment regions. Although we focus here on applications at smaller scale OBS arrays, the methodology can be extended to similarly sized arrays in continental settings. For larger arrays such as the USArray, one could estimate 1-D attenuation within “subarrays” representing regions that are expected to contain little lateral heterogeneity. Additional synthetic testing using realistic wave propagation through laterally varying 3-D anelastic media is required to evaluate the ability to reliably resolve lateral variations in Rayleigh wave attenuation within larger arrays.

6.2. Comparison to Previous Attenuation Studies

While our new observations of shear attenuation at NoMelt and JdF broadly resemble previous observations, important differences do exist. The approximate two-layer structure that we observe at NoMelt with a transition from low to high attenuation at 50–100 km depth is consistent with the two-layer model of Ma et al. (2020) with the lithosphere–asthenosphere boundary at 70 km depth; however, in the earlier study the asthenospheric layer shows lower attenuation ($Q_\mu \sim 110$) than we find here ($Q_\mu \sim 50$ to 70), which underpredicts our Rayleigh wave attenuation observations at periods >25 s (blue dashed line in Figure 11b). Compared to the NoMelt region in global model QRFSI12 (Dalton et al., 2008), our NoMelt model is slightly less attenuating from 50 to 150 km and is slightly more attenuating from 200 to 250 km. However, the general agreement is exceptional given the broad sensitivities associated with global modeling compared to our local estimates.

The high attenuation peak at 100–130 km depth that we observe at JdF resembles that of Ruan et al. (2018), but the attenuation peak in their model is both shallower (50–100 km) and stronger ($Q_\mu \sim 46$), overpredicting our attenuation observations for periods <60 s (red dashed line in Figure 11b). The deeper high attenuation region in our model is more consistent with body-wave observations that imply a low viscosity melt column extending to ~150 km below the JdF Ridge (Eilon & Abers, 2017). The low attenuation region at >200 km depth in our model ($Q_\mu > 200$) appears less attenuating than Ruan et al. (2018) at first glance, but values are consistent to within uncertainty (see their Figure 2c). Our observations agree well with QRFSI12 at depths of 50–150 km, but we observe lower attenuation from 200 to 250 km.

Differences between our estimates of Q_μ at NoMelt and JdF and previous observations are primarily related to inconsistencies in the Rayleigh wave attenuation measurements (Figure 10), rather than in the inversion procedure. This point is demonstrated by the large misfit between previous model predictions of Rayleigh wave attenuation and our observations in Figure 11b. As the previous attenuation measurements of Ruan et al. (2018) and Ma et al. (2020) were made using the TPW method, a key question is whether these differences can be attributed to our use of Helmholtz tomography or whether they arise from the raw amplitude and/or phase measurements themselves. Our synthetic tests show that Helmholtz and TPW yield similar attenuation measurements (at periods >35 s, where focusing corrections are smaller), when applied to the same amplitude and phase data set (Figure 9). A similar result is found using the real data: Helmholtz and TPW attenuation measurements agree to within uncertainty when applied to the same amplitude and phase data set (pink symbols in Figure S3 in Supporting

Information S1). This suggests, albeit indirectly, that differences in our revised attenuation estimates arise from differences in the raw single-station amplitude measurements and/or event distribution and not the chosen theoretical framework used to interpret these amplitudes in terms of attenuation (i.e., Helmholtz vs. TPW). We use the cross-correlation based ASWMS tool of Jin and Gaherty (2015) to measure station amplitude and differential phase, while previous TPW studies used a single-station Fourier transform (FT) based method (Forsyth & Li, 2005) to measure amplitude and phase. Both techniques involve time windowing and narrow-band filtering of the waveform, but windowing in ASWMS is performed automatically based on broadband Rayleigh wave energy (narrow-band filtering occurs after cross-correlation), whereas for the FT method, narrow-band filters are applied before windowing and user input is required to manually select the edges of each window. Given these differences, it is difficult to determine at what stage in the measurement procedures the amplitude measurements might diverge. We emphasize that phase velocity measurements using ASWMS and FT are equivalent to within uncertainty (see Figure 4a in Ma et al. (2020)), indicating that phase is consistent between the two measurement techniques.

Both the Helmholtz and TPW methods applied to ASWMS amplitude and phase measurements are able to recover the true attenuation (and amplification) values from realistic SPECFEM3D GLOBE synthetic seismograms, providing confidence in our revised attenuation estimates at JdF and NoMelt. An advantage of our study is that we treat the JdF and NoMelt data sets identically throughout both the measurement and inversion procedures, and therefore, differences in attenuation observed between the two locations are driven strictly by the data and not by ad hoc choices made within the analysis. In a future study, we will interpret these updated profiles of Q_μ alongside profiles of shear velocity to quantify temperature, melt fraction, and grain size in the oceanic asthenosphere.

6.3. Site Amplification: A New Observable in the Oceans

Our observations of local site amplification, β , at JdF and NoMelt are among the first of their kind in an oceanic setting. Only a handful of previous studies have measured Rayleigh wave amplification at periods >20 s (Bao et al., 2016; Bowden et al., 2017; Eddy & Ekström, 2014, 2020; F. C. Lin et al., 2012), and these studies all used data from the USArray. One study that we are aware of has inverted Rayleigh wave amplification measurements for shear velocity structure, and this too was carried out in the western U.S. (Schardong et al., 2019). The sensitivities of Rayleigh wave amplification to shear velocity (V_S), compressional velocity (V_P), and density (ρ) are complementary to that of phase velocity and may be used to refine models of 3-D Earth structure (Bowden et al., 2017; F. C. Lin et al., 2012; Schardong et al., 2019). Amplification displays opposite sensitivities to shear and compressional velocities at shallow depths, implying that V_P/V_S may be especially well resolved by amplification measurements (F. C. Lin et al., 2012). In contrast to phase and group velocity, the amplification sensitivity kernels for V_S have multiple zero-crossings and therefore should better resolve sharp gradients in shear velocity with depth (Babikoff, 2022; Dalton & Babikoff, 2021; F. C. Lin et al., 2012).

Our synthetic recovery tests (Figures 6 and 7) and application to the real data sets (Figure 8) demonstrate that amplification can be measured a typical OBS array geometries using Helmholtz tomography. Strong amplification observed along the JdF Ridge approximately coincides with slow phase velocities (Figure 5f), indicating that they can be inverted together to refine shallow Earth structure. In particular, improved shallow estimates of V_P/V_S at the JdF Ridge could shed light on the organization of melt and crustal accretion processes as well as shallow cracks and hydrothermal circulation (Kim et al., 2019; Lee et al., 2017; Takei, 2002). We reemphasize that β is a relative quantity with mean value equal to one within the array, and thus, an inversion of amplification for structural parameters V_S , V_P , and ρ must also preserve the array average. Joint inversion of amplification and phase velocity maps for crust and mantle properties at JdF will be the topic of a future study.

7. Conclusions

This manuscript demonstrates application of Helmholtz attenuation tomography in an oceanic setting, yielding new measurements of Rayleigh wave attenuation and local site amplification at 20–150 s period at the NoMelt and JdF regions. Using realistic simulations of wave propagation through 3-D elastic structure, we show that the technique faithfully accounts for wavefield focusing and defocusing, including in extreme scenarios associated with coastline effects. The focusing and defocusing corrections measured using the real data set are qualitatively similar to the synthetics but are larger in amplitude, likely due to the smooth global model used to generate the

synthetic data set. The methodology has been implemented as an add-on to the ASWMS software package (Jin & Gaherty, 2015; see Data Availability Statement), offering a new tool for estimating Rayleigh wave attenuation and amplification across regional-scale arrays that has been validated using realistic synthetic seismograms. Although our focus is on applications at smaller scale OBS arrays ($\sim 500 \text{ km} \times 500 \text{ km}$), the technique can be extended to comparable data sets on land.

Both 1-D attenuation and 2-D site amplification are successfully recovered in the synthetic tests at NoMelt and JdF, indicating that the array geometries and earthquake distributions are sufficient for resolving tradeoffs between attenuation and site amplification. When applied to the real data, our measurements of Rayleigh wave attenuation at NoMelt and JdF revise previous estimates derived using the TPW method. Our preliminary inversions of Rayleigh wave attenuation for 1-D profiles of shear attenuation, Q_μ , reveal significantly higher attenuation in the asthenosphere at NoMelt and a deeper high-attenuation region at JdF compared to previous studies. Maps of site amplification at JdF show high amplification (>10% at 31 s period) along the low-velocity JdF Ridge, providing a new observable that can be inverted alongside phase velocity to improve models of shallow subsurface structure at the mid-ocean ridge.

Data Availability Statement

The methodology described in this manuscript is implemented as an add-on to the MATLAB-based Automated Surface-Wave Measurement System of Jin and Gaherty (2015) and is hosted on GitHub (<https://github.com/jbrussell/ASWMS-Q.git>); the Mapping Toolbox is required. The maps in Figure 1 were generated using the Python-based PyGMT software (<https://www.pygmt.org/>). The SPECFEM3D_GLOBE software used to generate the synthetic data sets can be downloaded here: https://github.com/geodynamics/specfem3d_globe.git. The Automated Tilt and Compliance Removal software can be accessed here: <https://github.com/helenjanisz/ATaCR.git>. Data used in this manuscript were retrieved from the Incorporated Research Institutions for Seismology (IRIS) Data Management Center (DMC) under network codes ZA (NoMelt) and 7D (Cascadia Initiative; Juan de Fuca).

Acknowledgments

The authors appreciate the science parties, captain and crew, and ocean-bottom seismometer instrument centers at WHOI, SIO, and LDEO who made possible the collection of the data used in this article. The authors thank Zhiyu Ma and Donald Forsyth for insightful discussions regarding the TPW method; Anant Hariharan for useful input about overtone interference; Helen Janiszewski for sharing Juan de Fuca plate boundary data; and Ge Jin and James Gaherty for developing and openly sharing/maintaining the ASWMS software, which was central to this study (see Data Availability Statement for the link to our modified ASWMS-Q code). The authors also thank Daniel Bowden, one anonymous reviewer, and the Associate Editor for helpful comments that improved this manuscript. This work was supported by an NSF EAR Postdoctoral Fellowship awarded to Russell (EAR-1952702) and Dalton was supported by the NSF Award EAR-2044136.

References

- Adenis, A., Debayle, E., & Ricard, Y. (2017a). Attenuation tomography of the upper mantle. *Geophysical Research Letters*, 44(15), 7715–7724. <https://doi.org/10.1002/2017GL073751>
- Adenis, A., Debayle, E., & Ricard, Y. (2017b). Seismic evidence for broad attenuation anomalies in the asthenosphere beneath the Pacific Ocean. *Geophysical Journal International*, 209(3), 1677–1698. <https://doi.org/10.1093/gji/ggx117>
- Babikoff, J. (2022). *Imaging the lithosphere and asthenosphere beneath North America with Rayleigh wave phase velocity and amplification*. Brown University.
- Bao, X., Dalton, C. A., Jin, G., Gaherty, J. B., & Shen, Y. (2016). Imaging Rayleigh wave attenuation with USArray. *Geophysical Journal International*, 206(1), 241–259. <https://doi.org/10.1093/gji/ggw151>
- Bassin, C., Laske, G., & Masters, G. (2000). The current limits of resolution for surface wave tomography in North America. *EOS Trans AGU*, 81, F897.
- Bell, S. W., Ruan, Y., & Forsyth, D. W. (2016). Ridge asymmetry and deep aqueous alteration at the trench observed from Rayleigh wave tomography of the Juan de Fuca plate. *Journal of Geophysical Research: Solid Earth*, 121(10), 7298–7321. <https://doi.org/10.1002/2016JB012990>.
- Received**
- Bowden, D. C., Tsai, V. C., & Lin, F. C. (2017). Amplification and attenuation across USArray using ambient noise waveform tracking. *Journal of Geophysical Research: Solid Earth*, 122(12), 10086–10101. <https://doi.org/10.1002/2017JB014804>
- Byrnes, J. S., Toomey, D. R., Hooft, E. E. E., Nábělek, J., & Braunmiller, J. (2017). Mantle dynamics beneath the discrete and diffuse plate boundaries of the Juan de Fuca plate: Results from Cascadia Initiative body wave tomography. *Geochemistry, Geophysics, Geosystems*, 18(8), 2906–2929. <https://doi.org/10.1002/2017GC006980>
- Chevrot, S., & Lehujeur, M. (2022). Eikonal surface wave tomography with smoothing splines—Application to southern California. *Geophysical Journal International*, 229(3), 1927–1941. <https://doi.org/10.1093/gji/ggac034>
- Crawford, W. C., & Webb, S. C. (2000). Identifying and removing tilt noise from low frequency (<0.1 Hz) seafloor vertical seismic data. *Bulletin of the Seismological Society of America*, 90(4), 952–963. <https://doi.org/10.1785/0119990121>
- Dalton, C. A., & Babikoff, J. (2021). Rayleigh wave amplification: Sensitivity to elastic structure and application to Alaskan crust and upper mantle. In *AGU Fall Meeting Abstracts*.
- Dalton, C. A., & Ekström, G. (2006). Global models of surface wave attenuation. *Journal of Geophysical Research*, 111(5), 1–19. <https://doi.org/10.1029/2005JB003997>
- Dalton, C. A., Ekström, G., & Dziewonski, A. M. (2008). The global attenuation structure of the upper mantle. *Journal of Geophysical Research*, 113(B9), 1–24. <https://doi.org/10.1029/2007JB005429>
- Dalton, C. A., & Faul, U. H. (2010). The oceanic and cratonic upper mantle: Clues from joint interpretation of global velocity and attenuation models. *Lithos*, 120(1–2), 160–172. <https://doi.org/10.1016/j.lithos.2010.08.020>
- Debayle, E., Bodin, T., Durand, S., & Ricard, Y. (2020). Seismic evidence for partial melt below tectonic plates. *Nature*, 586(7830), 555–559. <https://doi.org/10.1038/s41586-020-2809-4>
- Durek, J. J., & Ekström, G. (1996). A radial model of anelasticity consistent with long-period surface-wave attenuation. *Bulletin of the Seismological Society of America*, 86, 144–158.

- Dziewoński, A. M., & Anderson, D. L. (1981). Preliminary reference Earth model. *Physics of the Earth and Planetary Interiors*, 25(4), 297–356. [https://doi.org/10.1016/0031-9201\(81\)90046-7](https://doi.org/10.1016/0031-9201(81)90046-7)
- Eddy, C. L., & Ekström, G. (2014). Local amplification of Rayleigh waves in the continental United States observed on the USArray. *Earth and Planetary Science Letters*, 402, 50–57. <https://doi.org/10.1016/j.epsl.2014.01.013>
- Eddy, C. L., & Ekström, G. (2020). Comparisons between measurements and predictions of Rayleigh wave amplification across the contiguous United States. *Physics of the Earth and Planetary Interiors*, 299, 106407. <https://doi.org/10.1016/j.pepi.2019.106407>
- Eilon, Z. C., & Abers, G. A. (2017). High seismic attenuation at a mid-ocean ridge reveals the distribution of deep melt. *Science Advances*, 3(5), e1602829. <https://doi.org/10.1126/sciadv.1602829>
- Eilon, Z. C., & Forsyth, D. W. (2020). Depth-dependent azimuthal anisotropy beneath the Juan de Fuca plate system. *Journal of Geophysical Research: Solid Earth*, 125(8), e2020JB019477. <https://doi.org/10.1029/2020JB019477>
- Ekström, G., Nettles, M., & Dziewoński, A. M. (2012). The global CMT project 2004–2010: Centroid-moment tensors for 13,017 earthquakes. *Physics of the Earth and Planetary Interiors*, 200–201, 1–9. <https://doi.org/10.1016/j.pepi.2012.04.002>
- Faul, U. H., & Jackson, I. (2005). The seismological signature of temperature and grain size variations in the upper mantle. *Earth and Planetary Science Letters*, 234(1–2), 119–134. <https://doi.org/10.1029/2001jb001225>
- Forsyth, D. W., & Li, A. (2005). Array analysis of two-dimensional variations in surface wave phase velocity and azimuthal anisotropy in the presence of multipathing interference. *Seismic Earth: Array Analysis of Broadband Seismograms Geophysical Monograph Series*, 157, 81–97.
- Hariharan, A., Dalton, C. A., Babikoff, J., & Ekström, G. (2022). Controls on surface wave overtone interference. *Geophysical Journal International*, 228(3), 1665–1683. <https://doi.org/10.1093/gji/gjab424>
- Hariharan, A., Dalton, C. A., Ma, Z., & Ekström, G. (2020). Evidence of overtone interference in fundamental-mode Rayleigh wave phase and amplitude measurements. *Journal of Geophysical Research: Solid Earth*, 125, 1–17. <https://doi.org/10.1029/2019JB018540>
- Havlin, C., Holtzman, B. K., & Hopper, E. (2021). Inference of thermodynamic state in the asthenosphere from anelastic properties, with applications to North American upper mantle. *Physics of the Earth and Planetary Interiors*, 314, 106639. <https://doi.org/10.1016/j.pepi.2020.106639>
- Hawley, W. B., Allen, R. M., & Richards, M. A. (2016). Tomography reveals buoyant asthenosphere accumulating beneath the Juan de Fuca plate. *Science*, 353(6306), 1406–1408. <https://doi.org/10.1126/science.aad8104>
- Jackson, I., & Faul, U. H. (2010). Grainsize-sensitive viscoelastic relaxation in olivine: Towards a robust laboratory-based model for seismological application. *Physics of the Earth and Planetary Interiors*, 183(1–2), 151–163. <https://doi.org/10.1016/j.pepi.2010.09.005>
- Janiszewski, H. A., Gaherty, J. B., Abers, G. A., Gao, H., & Eilon, Z. C. (2019). Amphibious surface-wave phase-velocity measurements of the Cascadia subduction zone. *Geophysical Journal International*, 217(3), 1929–1948. <https://doi.org/10.1093/gji/gjz051>
- Jin, G., & Gaherty, J. B. (2015). Surface wave phase-velocity tomography based on multichannel cross-correlation. *Geophysical Journal International*, 201(3), 1383–1398. <https://doi.org/10.1093/gji/gjv079>
- Karaoglu, H., & Romanowicz, B. (2018). Inferring global upper-mantle shear attenuation structure by waveform tomography using the spectral element method. *Geophysical Journal International*, 213(3), 1536–1558. <https://doi.org/10.1093/gji/ggy030>
- Kim, E., Toomey, D. R., Hooft, E. E. E., Wilcock, W. S. D., Weekly, R. T., Lee, S. M., & Kim, Y. H. (2019). Upper crustal Vp/Vs ratios at the Endeavour segment, Juan de Fuca ridge, from joint inversion of P and S traveltimes: Implications for hydrothermal circulation. *Geochemistry, Geophysics, Geosystems*, 20(1), 208–229. <https://doi.org/10.1029/2018GC007921>
- Komatitsch, D., & Tromp, J. (2002a). Spectral-element simulations of global seismic wave propagation—I. Validation. *Geophysical Journal International*, 149(2), 390–412. <https://doi.org/10.1046/j.1365-246X.2002.01653.x>
- Komatitsch, D., & Tromp, J. (2002b). Spectral-element simulations of global seismic wave propagation—II. Three-dimensional models, oceans, rotation and self-gravitation. *Geophysical Journal International*, 150(2), 303–318. <https://doi.org/10.1046/j.1365-246X.2002.01653.x>
- Kustowski, B., Ekstro, G., & Dziewoński, A. M. (2008). Anisotropic shear-wave velocity structure of the Earth's mantle: A global model. *Journal of Geophysical Research*, 113(B6), 1–23. <https://doi.org/10.1029/2007JB005169>
- Langston, C. A. (2007a). Spatial gradient analysis for linear seismic arrays. *Bulletin of the Seismological Society of America*, 97(1 B), 265–280. <https://doi.org/10.1785/0120060100>
- Langston, C. A. (2007b). Wave gradiometry in the time domain. *Bulletin of the Seismological Society of America*, 97(3), 926–933. <https://doi.org/10.1785/0120060152>
- Langston, C. A. (2007c). Wave gradiometry in two dimensions. *Bulletin of the Seismological Society of America*, 97(2), 401–416. <https://doi.org/10.1785/0120060138>
- Lee, A. L., Walker, A. M., Lloyd, G. E., & Torvela, T. (2017). Modeling the impact of melt on seismic properties during mountain building. *Geochemistry, Geophysics, Geosystems*, 18(3), 1090–1110. <https://doi.org/10.1002/2016GC006705.Received>
- Lin, F.-C., & Ritzwoller, M. H. (2011). Helmholtz surface wave tomography for isotropic and azimuthally anisotropic structure. *Geophysical Journal International*, 186(3), 1104–1120. <https://doi.org/10.1111/j.1365-246X.2011.05070.x>
- Lin, F.-C., Ritzwoller, M. H., & Snieder, R. (2009). Eikonal tomography: Surface wave tomography by phase front tracking across a regional broad-band seismic array. *Geophysical Journal International*, 177(3), 1091–1110. <https://doi.org/10.1111/j.1365-246X.2009.04105.x>
- Lin, F. C., Tsai, V. C., & Ritzwoller, M. H. (2012). The local amplification of surface waves: A new observable to constrain elastic velocities, density, and anelastic attenuation. *Journal of Geophysical Research*, 117(6), 1–20. <https://doi.org/10.1029/2012JB009208>
- Lin, P.-Y. P., Gaherty, J. B., Jin, G., Collins, J. A., Lizarralde, D., Evans, R. L., & Hirth, G. (2016). High-resolution seismic constraints on flow dynamics in the oceanic asthenosphere. *Nature*, 535(7613), 1–9. <https://doi.org/10.1038/nature18012>
- Liu, H., Anderson, D. L., & Kanamori, H. (1976). Velocity dispersion due to anelasticity; implications for seismology and mantle composition. *Geophysical Journal of the Royal Astronomical Society*, 47(1), 41–58. <https://doi.org/10.1111/j.1365-246X.1976.tb01261.x>
- Liu, Y., & Holt, W. E. (2015). Wave gradiometry and its link with Helmholtz equation solutions applied to USArray in the eastern U.S. *Journal of Geophysical Research: Solid Earth*, 120(8), 5717–5746. <https://doi.org/10.1002/2015JB011982>
- Ma, Z., Dalton, C. A., Russell, J. B., Gaherty, J. B., Hirth, G., & Forsyth, D. W. (2020). Shear attenuation and anelastic mechanisms in the central Pacific upper mantle. *Earth and Planetary Science Letters*, 536, 116148. <https://doi.org/10.1016/j.epsl.2020.116148>
- Mark, H. F., Collins, J. A., Lizarralde, D., Hirth, G., Gaherty, J. B., Evans, R. L., & Behn, M. D. (2021). Constraints on the depth, thickness, and strength of the G discontinuity in the central Pacific from S receiver functions. *Journal of Geophysical Research: Solid Earth*, 126(4), e2019JB019256. <https://doi.org/10.1029/2019JB019256>
- Mark, H. F., Lizarralde, D., Collins, J. A., Miller, N. C., Hirth, G., Gaherty, J. B., & Evans, R. L. (2019). Azimuthal seismic anisotropy of 70-Ma Pacific-plate upper mantle. *Journal of Geophysical Research: Solid Earth*, 124(2), 1889–1909. <https://doi.org/10.1029/2018JB016451>
- McCarthy, C., & Takei, Y. (2011). Anelasticity and viscosity of partially molten rock analogue: Toward seismic detection of small quantities of melt. *Geophysical Research Letters*, 38(18), 3–7. <https://doi.org/10.1029/2011GL048776>
- McCarthy, C., Takei, Y., & Hiraga, T. (2011). Experimental study of attenuation and dispersion over a broad frequency range: 2. The universal scaling of polycrystalline materials. *Journal of Geophysical Research*, 116(9), 1–18. <https://doi.org/10.1029/2011JB008384>

- Priestley, K., & McKenzie, D. (2013). The relationship between shear wave velocity, temperature, attenuation and viscosity in the shallow part of the mantle. *Earth and Planetary Science Letters*, 381, 78–91. <https://doi.org/10.1016/j.epsl.2013.08.022>
- Richards, F. D., Hoggard, M. J., White, N., & Ghelichkhan, S. (2020). Quantifying the relationship between short-wavelength dynamic topography and thermomechanical structure of the upper mantle using calibrated parameterization of anelasticity. *Journal of Geophysical Research: Solid Earth*, 125(9). <https://doi.org/10.1029/2019JB019062>
- Ruan, Y., Forsyth, D. W., & Bell, S. W. (2018). Shear attenuation beneath the Juan de Fuca plate: Implications for mantle flow and dehydration. *Earth and Planetary Science Letters*, 496, 189–197. <https://doi.org/10.1016/j.epsl.2018.05.035>
- Russell, J. B., & Gaherty, J. B. (2021). Lithospheric structure and seismic anisotropy offshore Eastern North America: Implications for continental breakup and ultra-slow spreading dynamics. *Journal of Geophysical Research: Solid Earth*, 126(12), e2021JB022955. <https://doi.org/10.1029/2021JB022955>
- Russell, J. B., Gaherty, J. B., Lin, P.-Y. P., Lizarralde, D., Collins, J. A., Hirth, G., & Evans, R. L. (2019). High-resolution constraints on Pacific upper mantle petrofabric inferred from surface-wave anisotropy. *Journal of Geophysical Research: Solid Earth*, 124(1), 631–657. <https://doi.org/10.1029/2018JB016598>
- Russell, J. B., Gaherty, J. B., Mark, H. F., Hirth, G., Hansen, L. N., Lizarralde, D., et al. (2022). Seismological evidence for girdled olivine lattice-preferred orientation in oceanic lithosphere and implications for mantle deformation processes during seafloor spreading. *Geochemistry, Geophysics, Geosystems*. <https://doi.org/10.1029/2022gc010542>
- Saikia, U., Rychert, C. A., Harmon, N., & Michael Kendall, J. (2021). Seismic attenuation at the Equatorial mid-Atlantic ridge constrained by local Rayleigh wave analysis from the PI-LAB Experiment. *Geochemistry, Geophysics, Geosystems*, 22(12), 1–16. <https://doi.org/10.1029/2021GC010085>
- Sarafian, E., Evans, R. L., Collins, J. A., Elsenbeck, J., Gaetani, G. A., Gaherty, J. B., et al. (2015). The electrical structure of the central Pacific upper mantle constrained by the NoMelt experiment. *Geochemistry, Geophysics, Geosystems*, 16(4), 1115–1132. <https://doi.org/10.1002/2014GC005709.Received>
- Schardong, L., Ferreira, A. M. G., Berbellini, A., & Sturgeon, W. (2019). The anatomy of uppermost mantle shear-wave speed anomalies in the western U.S. from surface-wave amplification. *Earth and Planetary Science Letters*, 528, 115822. <https://doi.org/10.1016/j.epsl.2019.115822>
- Seton, M., Müller, R. D., Zahirovic, S., Williams, S., Wright, N. M., Cannon, J., et al. (2020). A global data set of present-day oceanic crustal age and seafloor spreading parameters. *Geochemistry, Geophysics, Geosystems*, 21(10), e2020GC009214. <https://doi.org/10.1029/2020GC009214>
- Takei, Y. (2002). Effect of pore geometry on V_p/V_s : From equilibrium geometry to crack. *Journal of Geophysical Research*, 107(B2), 2043. <https://doi.org/10.1029/2001jb000522>
- Tromp, J., & Dahlen, F. A. (1992). Variational principles for surface wave propagation on a laterally heterogeneous Earth-III. Potential representation. *Geophysical Journal International*, 112(2), 195–209. <https://doi.org/10.1111/j.1365-246X.1993.tb01449.x>
- Uieda, L., Tian, D., Leong, W. J., Jones, M., Schlitzer, W., Grund, M., et al. (2022). PyGMT: A Python interface for the Generic Mapping Tools (Version v0.7.0) [Computer software]. Zenodo.<https://doi.org/10.5281/ZENODO.6702566>
- Webb, S. C., & Crawford, W. C. (1999). Long-period seafloor seismology and deformation under ocean waves. *Bulletin of the Seismological Society of America*, 89(6), 1535–1542. <https://doi.org/10.1785/bssa0890061535>
- Yamauchi, H., & Takei, Y. (2016). Polycrystal anelasticity at near-solidus temperatures. *Journal of Geophysical Research: Solid Earth*, 121(11), 7790–7820. <https://doi.org/10.1002/2016JB013316>
- Yang, Y., & Forsyth, D. W. (2006). Regional tomographic inversion of the amplitude and phase of Rayleigh waves with 2-D sensitivity kernels. *Geophysical Journal International*, 166(3), 1148–1160. <https://doi.org/10.1111/j.1365-246x.2006.02972.x>